Acta Biomaterialia 60 (2017) 315–329

Contents lists available at ScienceDirect

Acta Biomaterialia

journal homepage: www.elsevier.com/locate/actabiomat

Full length article

Rheological characterization of human brain tissue

S. Budday [a], G. Sommer [b], J. Haybaeck [c,d], P. Steinmann [a], G.A. Holzapfel [b,e], E. Kuhl [f,*]

[a] Department of Mechanical Engineering, University of Erlangen-Nuremberg, 91058 Erlangen, Germany
[b] Institute of Biomechanics, Graz University of Technology, 8010 Graz, Austria
[c] Department of Neuropathology, Medical University of Graz, 8036 Graz, Austria
[d] Department of Pathology, Otto-von-Guericke University Magdeburg, 39120 Magdeburg, Germany
[e] Norwegian University of Science and Technology, Faculty of Engineering Science and Technology, 7491 Trondheim, Norway
[f] Departments of Mechanical Engineering & Bioengineering, Stanford University, CA 94305, USA

ARTICLE INFO

Article history:
Received 3 March 2017
Received in revised form 3 June 2017
Accepted 15 June 2017
Available online 26 June 2017

Keywords:
Human brain
Rheological testing
Finite viscoelasticity
Ogden model
Parameter identification

ABSTRACT

The rheology of ultrasoft materials like the human brain is highly sensitive to regional and temporal variations and to the type of loading. While recent experiments have shaped our understanding of the time-independent, hyperelastic response of human brain tissue, its time-dependent behavior under various loading conditions remains insufficiently understood. Here we combine cyclic and relaxation testing under multiple loading conditions, shear, compression, and tension, to understand the rheology of four different regions of the human brain, the cortex, the basal ganglia, the corona radiata, and the corpus callosum. We establish a family of finite viscoelastic Ogden-type models and calibrate their parameters simultaneously for all loading conditions. We show that the model with only one viscoelastic mode and a constant viscosity captures the essential features of brain tissue: nonlinearity, pre-conditioning, hysteresis, and tension-compression asymmetry. With stiffnesses and time constants of $\mu_\infty = 0.7$ kPa, $\mu_1 = 2.0$ kPa, and $\tau_1 = 9.7$ s in the gray matter cortex and $\mu_\infty = 0.3$ kPa, $\mu_1 = 0.9$ kPa and $\tau_1 = 14.9$ s in the white matter corona radiata combined with negative parameters α_∞ and α_1, this five-parameter model naturally accounts for pre-conditioning and tissue softening. Increasing the number of viscoelastic modes improves the agreement between model and experiment, especially across the entire relaxation regime. Strikingly, two cycles of pre-conditioning decrease the gray matter stiffness by up to a factor three, while the white matter stiffness remains almost identical. These new insights allow us to better understand the rheology of different brain regions under mixed loading conditions. Our family of finite viscoelastic Ogden-type models for human brain tissue is simple to integrate into standard nonlinear finite element packages. Our simultaneous parameter identification of multiple loading modes can inform computational simulations under physiological conditions, especially at low to moderate strain rates. Understanding the rheology of the human brain will allow us to more accurately model the behavior of the brain during development and disease and predict outcomes of neurosurgical procedures.

Statement of Significance

While recent experiments have shaped our understanding of the time-independent, hyperelastic response of human brain tissue, its time-dependent behavior at finite strains and under various loading conditions remains insufficiently understood. In this manuscript, we characterize the rheology of human brain tissue through a family of finite viscoelastic Ogdentype models and identify their parameters for multiple loading modes in four different regions of the brain. We show that even the simplest model of this family, with only one viscoelastic mode and five material parameters, naturally captures the essential features of brain tissue: its characteristic nonlinearity, pre-conditioning, hysteresis, and tension-compression asymmetry. For the first time, we simultaneously identify a single parameter set for shear, compression, tension, shear relaxation, and compression relaxation loading. This parameter set is significant for computational simulations under physiological conditions, where loading is naturally of mixed mode nature. Understanding the rheology of the human brain will help us predict neurosurgical procedures, inform brain injury criteria, and improve the design of protective devices.

* Corresponding author.
E-mail address: ekuhl@stanford.edu (E. Kuhl).

http://dx.doi.org/10.1016/j.actbio.2017.06.024
1742-7061/

1. Introduction

The rheology of the human brain plays an important role in brain function and failure [1]. With the opportunity to develop personalized three-dimensional human head models [2], computational simulations are promising tools to predict mechanically mediated pathways of brain damage [3] and to improve neurosurgical procedures [4]. The quality of numerical predictions critically relies on accurate constitutive models and, equally importantly, on the thorough calibration of their model parameters [5]. Model calibration is extremely challenging since the rheology of materials like the brain strongly depends on the spatial and temporal scales of interest [6]. Variations in experimental protocols, loading modes, loading rates, and spatial resolution have generated contradictory results both qualitatively and quantitatively [7]. Clearly, to develop an appropriate rheological model, it is essential to understand the loading-mode specific, time-dependent material response. Even for quasi-static loading rates, brain tissue exhibits a highly nonlinear, conditioning, hysteretic, and tension-compression asymmetric behavior [8–10]. While several studies have identified the linear viscoelastic material parameters of human brain tissue at small strains and under a single loading mode [11–15], time-dependent phenomena at finite strains and under arbitrary loading conditions remain less well characterized. So far, large strain viscoelastic constitutive models have only been calibrated for porcine brain under a single loading mode [16–18], but not for human brain under multiple loading modes. The objective of this study is therefore to establish a finite strain, nonlinear, viscoelastic constitutive model that captures the response of human brain tissue under various loading conditions. We performed simple shear, unconfined compression, tension, and stress relaxation in shear and compression and simultaneously calibrated the model for all five loading conditions. To eliminate inter-specimen variations, we performed all five tests sequentially on one and the same specimen.

Characterizing brain tissue is complicated by the highly heterogeneous microstructure with cell composition and morphology varying from one location to the other. While early studies have used large samples to include tissues of different types [11–14,19,20], recent studies have tried to characterize regionally varying tissue stiffness; yet, with controversial results: some studies reported cortical gray matter to be stiffer than white matter [21,10], others found the opposite [22–25]. A possible explanation for these seemingly contradictory observations could be that regional stiffness variations are time-dependent [10]. Here, we choose a small enough sample size to harvest homogeneous specimens from four different regions of the brain regions: the outer gray matter of the cortex, the inner gray matter of the basal ganglia, the white matter of the corona radiata, and the white matter of the corpus callosum that connects the two hemispheres. We systematically compare the region-specific elastic and viscous material parameters to ultimately characterize the human brain across space and time.

The most popular approach to characterize the time-dependent behavior of brain tissue is to use a Prony series [8,15,19,20,23,26,27], which is equivalent to a generalized Maxwell model for linear viscoelasticity in relaxation type loading [28]. The Prony series approach has two major limitations: it is restricted to linear elasticity and is computationally expensive [29]. To account for the large deformability of brain tissue, we consider a class of viscoelastic models within the general setting of finite deformation continuum mechanics. We adopt a fully nonlinear approach, which has previously been used to characterize the finite viscoelasticity of porcine brain under a single loading mode [16–18]. This implies that we multiplicatively decompose the deformation gradient into elastic and inelastic parts [30], and additively decompose the free energy function into an equilibrium and non-equilibrium parts [31]. We introduce internal variables to account for the rate-dependent behavior, and integrate the viscous rate equation in time using an operator split based on an exponential mapping [32].

The time-dependent rheology of brain tissue is associated with various physical mechanisms and time scales: The motion of fluid within the solid network of cells and extracellular matrix introduces a poroelastic behavior [9] whereas intracellular interactions between cytoplasm, nucleus, and cell membrane trigger a viscoelastic response [33]. In this study, we identify individual parameter sets for the unconditioned and conditioned tissue responses and discuss the differences in both parameter sets in view of a possible poroelastic and viscoelastic origin of time-dependent effects [34].

2. Materials and methods

2.1. Brain specimens

This study is based on $n = 10$ human brain samples described in detail in our previous study [10]. Fig. 1 illustrates representative coronal slices of all ten brains including the corpus callosum, the corona radiata, the basal ganglia, and the cortex.

Table 1 summarizes the characteristics of all tested brains. None of the subjects had suffered from any neurological disease known to affect the microstructure of the brain. We kept the tissue refrigerated at 3 °C and humidified with phosphate-buffered saline solution at all times to minimize tissue degradation. We tested all samples within 48 h after subject acquisition. This resulted in a total post mortem interval between death and the end of biomechanical testing of less than 60 h [10].

2.2. Specimen preparation

To characterize regional variations in tissue rheology, we differentiate between four regions: the corpus callosum (CC), the inner white matter connecting the two hemispheres; the corona radiata

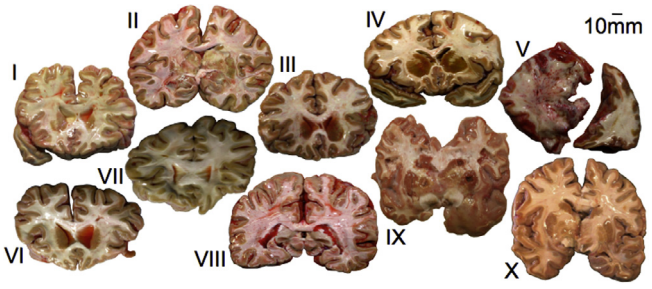

Fig. 1. Collection of the ten tested human brain slices.

Table 1
Sample characteristics: brain number, age, gender, and tested regions.

Brain number	Age years	Gender	Regions tested
I	69	male	CC,CR,BG,C
II	54	female	CC,CR,BG,C
III	63	male	CC,CR,BG,C
IV	63	male	CC,CR,BG,C
V	81	female	CR,C
VI	55	female	CC,CR,BG,C
VII	63	male	CC,CR,C
VII	68	male	CC,CR,BG,C
IX	78	male	CC,CR,BG,C
X	68	male	CC,CR,BG,C

CC = corpus callosum; CR = corona radiata; BG = basal ganglia; C = cortex.

(CR), the outer white matter; the basal ganglia (BG), the inner gray matter; and the cortex (C), the outer gray matter [10]. We chose specimen dimensions of 5 × 5 × 5 mm, restricted by the maximum cortical thickness of 5 mm. Due to the ultrasoft nature of brain tissue, the samples deformed under their own weight during preparation and mounting. This caused a variation in final sample dimensions with an edge length ranging from 3 to 7 mm and a specimen height ranging from 2 to 5 mm. To limit tissue degradation, we excised and prepared each sample shortly before testing and humidified the specimens with phosphate-buffered saline solution to avoid tissue dehydration.

2.3. Experimental setup

After extraction and preparation, we glued each sample to the upper specimen holder as illustrated in Fig. 2a and b. Prior to testing, we measured the dimensions of each sample to characterize the reference configuration to calculate the stretch, shear, and stresses during loading. We mounted the specimens in the triaxial testing device, provided a thin layer of adhesive to the lower specimen holder, and lowered the sample until we detected a preload of 10 mN. After a hardening period of 300 s, we slowly reduced the preload to 0 mN, adjusted the relative position of the plates in *x*- and *y*-directions, and zeroed the forces. This is the state that we defined as the reference configuration [10], as illustrated in Fig. 2c. Before starting the actual test, we humidified the sample with phosphate-buffered saline solution as shown in Fig. 2d.

We conducted all tests at room temperature. The system operates with a stroke resolution of 0.04 µm in the *z*-direction and with a stroke resolution of 0.25 µm in the *x*- and *y*-directions [35]. We recorded the resulting forces with a three-axes force-sensor (K3D40, ME-Measuring Equipment, Henningsdorf, Germany). For motor control and data acquisition, we used the software testXpert II Version 3.2 (Zwick/Roell GmbH & Co. KG, Ulm, Germany) on a Windows-based personal computer.

2.4. Testing protocol

Table 2 summarizes our testing protocol. For each specimen, we performed a sequence of different loading modes, shear, compression, and tension [10]. For each loading mode, we applied three cycles and interpret the first cycle as the unconditioned and the third cycle as the conditioned response. First, we performed a simple shear test with a sinusoidal shear of up to $\gamma = 0.2$ under quasi-static conditions at a loading speed of $v = 2$ mm/min. Then, we performed a stress relaxation test under simple shear conditions with a rapid shear of $\gamma = 0.2$ at a speed of $v = 100$ mm/min and recorded the resulting forces for a period of 300 s. To limit preconditioning effects, we performed both tests in two orthogonal directions. Next, we performed an unconfined uniaxial compression test with $\lambda = 0.9$ compressive stretch, a relaxation test with $\lambda = 0.9$ compression for 300 s holding time, and a uniaxial tension test with $\lambda = 1.1$ tensile stretch. Since the recorded tensile forces were extremely low, the data were too noisy to record reasonable results for relaxation tests under tensile loading.

Table 2
Testing protocol.

Protocol: Sequence of multiple loading modes
• **Simple shear in x-direction** up to $\gamma = 0.2$ 2 pre-conditioning cycles + 1 main cycle
• **Stress relaxation in x-direction** at $\gamma = 0.2$ 300 s holding
• **Simple shear in y-direction** up to $\gamma = 0.2$ 2 pre-conditioning cycles + 1 main cycle
• **Stress relaxation in y-direction** at $\gamma = 0.2$ 300 s holding
• **Unconfined compression in z-direction** to $\lambda = 0.9$ 2 pre-conditioning cycles + 1 main cycle
• **Stress relaxation in z-direction** at $\lambda = 0.9$ 300 s holding
• **Uniaxial tension in z-direction** up to $\lambda = 1.1$ 2 pre-conditioning cycles + 1 main cycle

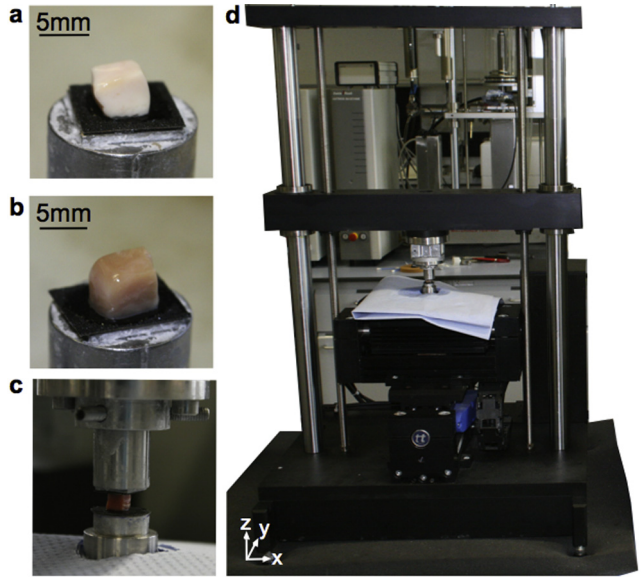

Fig. 2. a) White matter sample glued to upper specimen holder; b) gray matter brain sample glued to upper specimen holder; c) sample glued to upper and lower specimen holders of triaxial testing device; d) specimen mounted into testing device, hydrated with phosphate-buffered saline solution, and ready for testing.

3. Data analysis

In total, we analyzed data from $n = 58$ samples: $n = 13$ from the cortex, $n = 15$ from the basal ganglia, $n = 19$ from the corona radiata, and $n = 11$ from the corpus callosum [10].

3.1. Loading modes

To characterize the deformation during testing, we use the nonlinear equations of continuum mechanics and introduce the deformation map $\boldsymbol{\varphi}(\mathbf{X}, t)$, which maps the specimen from the undeformed, unloaded configuration with position vectors $\mathbf{X}$ at time t_0 to the deformed, loaded configuration with position vectors $\mathbf{x} = \boldsymbol{\varphi}(\mathbf{X}, t)$ at time t. The deformation gradient, $\mathbf{F} = \mathrm{d}\boldsymbol{\varphi}/\mathrm{d}\mathbf{X} = \nabla_{\mathbf{X}}\boldsymbol{\varphi}$, takes the following spectral representation,

$$\mathbf{F} = \nabla_{\mathbf{X}}\boldsymbol{\varphi} = \sum_{a=1}^{3} \lambda_a \, \mathbf{n}_a \otimes \mathbf{N}_a, \tag{1}$$

where λ_a are the eigenvalues and $\mathbf{n}_a = \mathbf{F} \cdot \mathbf{N}_a$ and $\mathbf{N}_a$ are the eigenvectors in the deformed and undeformed configurations. We apply two types of loading, simple shear and uniaxial compression/tension, and assume that the brain samples deform isochorically, $J = \det(\mathbf{F}) = \lambda_1\lambda_2\lambda_3 = 1$, and homogeneously.

3.1.1. Simple shear

To quantify the shear response of each specimen, we analyze the amount of shear γ and the corresponding Piola stresses P_{xz} and P_{yz}. We assume that the cross-section of the specimen remains unchanged and determine the shear stress $P_{xz} = \tau_{xz} = f/A$ or $P_{yz} = \tau_{yz} = f/A$ as the shear force f, the force recorded in the direction of shear, divided by the initial shear area $A = WL$, the product

of specimen length L and width W. The deformation gradient $\mathbf{F}$ for simple shear in the first direction takes the matrix representation,

$$\mathbf{F} = \begin{bmatrix} 1 & 0 & \gamma \\ 0 & 1 & 0 \\ 0 & 0 & 1 \end{bmatrix}, \tag{2}$$

and introduces the principal stretches

$$\lambda_{1/2} = \frac{\gamma}{2} \pm \sqrt{1 + \frac{\gamma^2}{4}} \quad \text{and} \quad \lambda_3 = 1. \tag{3}$$

3.1.2. Uniaxial compression and tension

To quantify uniaxial compression and tension, we analyze the stretch λ and the corresponding Piola stress P_{zz}. We determine the stretch $\lambda = 1 + \Delta z/H$ in terms of the specimen height H and z-displacement Δz. The Piola stress $P_{zz} = f_z/A$ is the force f_z divided by the initial cross-sectional area A in the unloaded reference configuration. The deformation gradient $\mathbf{F}$ for compression and tension takes the matrix representation

$$\mathbf{F} = \begin{bmatrix} 1/\sqrt{\lambda} & 0 & 0 \\ 0 & 1/\sqrt{\lambda} & 0 \\ 0 & 0 & \lambda \end{bmatrix}, \tag{4}$$

and introduces the principal stretches

$$\lambda_1 = \lambda_2 = \frac{1}{\sqrt{\lambda}} \quad \text{and} \quad \lambda_3 = \lambda. \tag{5}$$

3.2. Kinematics

Using the principal stretches for shear (3) or compression and tension (5), we can introduce the spectral representation of the right and left Cauchy-Green deformation tensors,

$$\begin{aligned} \mathbf{C} &= \mathbf{F}^{\mathrm{t}} \cdot \mathbf{F} = \sum_{\mathrm{a}=1}^{3} \lambda_{\mathrm{a}}^2 \mathbf{N}_{\mathrm{a}} \otimes \mathbf{N}_{\mathrm{a}} \\ \mathbf{b} &= \mathbf{F} \cdot \mathbf{F}^{\mathrm{t}} = \sum_{\mathrm{a}=1}^{3} \lambda_{\mathrm{a}}^2 \mathbf{n}_{\mathrm{a}} \otimes \mathbf{n}_{\mathrm{a}}, \end{aligned} \tag{6}$$

in terms of the undeformed and deformed eigenvectors $\mathbf{N}_{\mathrm{a}}$ and $\mathbf{n}_{\mathrm{a}}$. To model the viscoelastic nature of brain tissue, we decompose the deformation gradient into elastic and viscous parts,

$$\mathbf{F} = \mathbf{F}_i^{\mathrm{e}} \cdot \mathbf{F}_i^{\mathrm{v}} \qquad \forall \quad i = 1, .., m, \tag{7}$$

where i denotes a parallel arrangement of m viscoelastic modes [30]. It proves convenient to introduce the viscous right and elastic left Cauchy-Green deformation tensors $\mathbf{C}_i^{\mathrm{v}}$ and $\mathbf{b}_i^{\mathrm{e}}$ for each mode,

$$\begin{aligned} \mathbf{C}_i^{\mathrm{v}} &= (\mathbf{F}_i^{\mathrm{v}})^{\mathrm{t}} \cdot \mathbf{F}_i^{\mathrm{v}} = \mathbf{F}^{\mathrm{t}} \cdot (\mathbf{b}_i^{\mathrm{e}})^{-1} \cdot \mathbf{F} \\ \mathbf{b}_i^{\mathrm{e}} &= \mathbf{F}_i^{\mathrm{e}} \cdot (\mathbf{F}_i^{\mathrm{e}})^{\mathrm{t}} = \sum_{\mathrm{a}=1}^{3} (\lambda_{i\mathrm{a}}^{\mathrm{e}})^2 \, \mathbf{n}_{i\mathrm{a}}^{\mathrm{e}} \otimes \mathbf{n}_{i\mathrm{a}}^{\mathrm{e}}, \end{aligned} \tag{8}$$

and express $\mathbf{b}_i^{\mathrm{e}}$ in its spectral representation in terms of the elastic principal stretches $\lambda_{i\mathrm{a}}^{\mathrm{e}}$ and elastic eigenvectors $\mathbf{n}_{i\mathrm{a}}^{\mathrm{e}}$ [32]. The isochoric parts of the elastic left Cauchy-Green deformation tensors,

$$\tilde{\mathbf{b}}_i^{\mathrm{e}} = (J_i^{\mathrm{e}})^{-2/3} \mathbf{b}_i^{\mathrm{e}} = \sum_{\mathrm{a}=1}^{3} (\tilde{\lambda}_{i\mathrm{a}}^{\mathrm{e}})^2 \, \mathbf{n}_{i\mathrm{a}}^{\mathrm{e}} \otimes \mathbf{n}_{i\mathrm{a}}^{\mathrm{e}}. \tag{9}$$

define the isochoric principal stretches, $\tilde{\lambda}_{i\mathrm{a}}^{\mathrm{e}} = (J_i^{\mathrm{e}})^{-1/3} \lambda_{i\mathrm{a}}^{\mathrm{e}}$, in terms of the elastic Jacobians $J_i^{\mathrm{e}} = \det(\mathbf{F}_i^{\mathrm{e}})$. To characterize the rate of deformation, we introduce the spatial velocity gradient, $\mathbf{l} = \mathrm{d}\mathbf{v}/\mathrm{d}\mathbf{x} = \nabla_{\mathbf{x}}\mathbf{v}$,

$$\mathbf{l} = \nabla_{\mathbf{x}}\mathbf{v} = \dot{\mathbf{F}} \cdot \mathbf{F}^{-1} = \mathbf{l}_i^{\mathrm{e}} + \mathbf{l}_i^{\mathrm{v}}, \tag{10}$$

and additively decompose it into an elastic part, $\mathbf{l}_i^{\mathrm{e}} = \dot{\mathbf{F}}^{\mathrm{e}} \cdot (\mathbf{F}_i^{\mathrm{e}})^{-1}$, and a viscous part, $\mathbf{l}_i^{\mathrm{v}} = \mathbf{F}_i^{\mathrm{e}} \cdot \dot{\mathbf{F}}_i^{\mathrm{v}} \cdot (\mathbf{F}_i^{\mathrm{v}})^{-1} \cdot (\mathbf{F}_i^{\mathrm{e}})^{-1}$. We further decompose these two contributions into their symmetric and skew-symmetric parts,

$$\mathbf{l}_i^{\mathrm{e}} = \mathbf{d}_i^{\mathrm{e}} + \mathbf{w}_i^{\mathrm{e}} \quad \text{and} \quad \mathbf{l}_i^{\mathrm{v}} = \mathbf{d}_i^{\mathrm{v}} + \mathbf{w}_i^{\mathrm{v}} \tag{11}$$

in terms of the stretch rates $\mathbf{d}_i = \frac{1}{2}[\mathbf{l}_i + (\mathbf{l}_i)^{\mathrm{t}}]$ and spin rates $\mathbf{w}_i = \frac{1}{2}[\mathbf{l}_i - (\mathbf{l}_i)^{\mathrm{t}}]$, and adopt the common assumption that the viscous deformation is spin-fee, $\mathbf{w}_i^{\mathrm{v}} \doteq \mathbf{0}$, i.e., $\mathbf{l}_i^{\mathrm{v}} \equiv \mathbf{d}_i^{\mathrm{v}}$.

3.3. Constitutive modeling

Motivated by our previous findings [10], we assume an isotropic material response for both the elastic and the viscoelastic behavior. We introduce a viscoelastic free energy function ψ as the sum of three terms [36], an equilibrium term ψ^{eq} in terms of the total principal stretches λ_{a}, a non-equilibrium term $\psi^{\mathrm{neq}} = \sum_{i=1}^{m} \psi_i$ in terms of the $i = 1, \ldots, m$ elastic principal stretches $\lambda_{i\mathrm{a}}^{\mathrm{e}}$, and a term $p[J-1]$ that enforces the incompressibility constraint, $J - 1 = 0$, via the Lagrange multiplier p,

$$\psi = \psi^{\mathrm{eq}} + \psi^{\mathrm{neq}} - p[J-1] \;\text{ with }\; \psi^{\mathrm{neq}} = \sum_{i=1}^{m} \psi_i(\mathbf{F}_i^{\mathrm{e}}). \tag{12}$$

The Kirchhoff stress $\boldsymbol{\tau}$ follows from standard arguments of thermodynamics and consists of three terms, the equilibrium term $\boldsymbol{\tau}^{\mathrm{eq}}$, the non-equilibrium term $\boldsymbol{\tau}^{\mathrm{neq}} = \sum_{i=1}^{m} \boldsymbol{\tau}_i$, and the volumetric term $-p\mathbf{I}$,

$$\tau = 2\,\frac{\partial \psi}{\partial \mathbf{b}} \cdot \mathbf{b} = \boldsymbol{\tau}^{\mathrm{eq}} + \boldsymbol{\tau}^{\mathrm{neq}} - p\mathbf{I} \;\text{ with }\; \boldsymbol{\tau}^{\mathrm{neq}} = \sum_{i=1}^{m} \boldsymbol{\tau}_i. \tag{13}$$

The hyperelastic response of brain tissue is best represented by the modified one-term Ogden model [37], with the strain energy function,

$$\psi^{\mathrm{eq}} = \frac{2\mu_\infty}{\alpha_\infty^2} \left[\lambda_1^{\alpha_\infty} + \lambda_2^{\alpha_\infty} + \lambda_3^{\alpha_\infty} - 3 \right] \tag{14}$$

where μ_∞ is the shear modulus and α_∞ is a second material parameter that characterizes tensioncompression asymmetry [10]. Knowing the total principal stretches λ_{a} from our displacement-controlled experiments, we can immediately calculate the equilibrium stress τ^{eq},

$$\boldsymbol{\tau}^{\mathrm{eq}} = 2\,\frac{\partial \psi^{\mathrm{eq}}}{\partial \mathbf{b}} \cdot \mathbf{b} = \sum_{\mathrm{a}=1}^{3} \frac{\partial \psi^{\mathrm{eq}}}{\partial \lambda_{\mathrm{a}}} \lambda_{\mathrm{a}} \, \mathbf{n}_{\mathrm{a}} \otimes \mathbf{n}_{\mathrm{a}}, \tag{15}$$

where $\partial \psi^{\mathrm{eq}}/\partial \lambda_{\mathrm{a}} = 2\mu_\infty \, \lambda_{\mathrm{a}}^{\alpha_\infty - 1}/\alpha_\infty$ for the Ogden model in Eq. (14). To determine the Kirchhoff stress $\boldsymbol{\tau}_i$ for each viscoelastic mode, we choose the same type of hyperelastic strain energy function for the non-equilibrium modes as for the equilibrium mode in (14),

$$\psi_i(\tilde{\lambda}_{i1}^{\mathrm{e}}, \tilde{\lambda}_{i2}^{\mathrm{e}}, \tilde{\lambda}_{i3}^{\mathrm{e}}) = \frac{2\mu_i}{\alpha_i^2} \left[(\tilde{\lambda}_{i1}^{\mathrm{e}})^{\alpha_i} + (\tilde{\lambda}_{i2}^{\mathrm{e}})^{\alpha_i} + (\tilde{\lambda}_{i3}^{\mathrm{e}})^{\alpha_i} - 3 \right], \tag{16}$$

but now parameterized in terms of the isochoric principal stretches $\tilde{\lambda}_{i\mathrm{a}}^{\mathrm{e}}$ from Eq. (9). We can then express the Kirchhoff stress of each mode,

$$\boldsymbol{\tau}_i = 2\,\frac{\partial \psi_i}{\partial \mathbf{b}_i^{\mathrm{e}}} \cdot \mathbf{b}_i^{\mathrm{e}} = \sum_{\mathrm{a}=1}^{3} \frac{\partial \psi_i}{\partial \lambda_{i\mathrm{a}}^{\mathrm{e}}} \lambda_{i\mathrm{a}}^{\mathrm{e}} \, \mathbf{n}_{i\mathrm{a}}^{\mathrm{e}} \otimes \mathbf{n}_{i\mathrm{a}}^{\mathrm{e}} = \sum_{\mathrm{a}=1}^{3} \tau_{i\mathrm{a}} \, \mathbf{n}_{i\mathrm{a}}^{\mathrm{e}} \otimes \mathbf{n}_{i\mathrm{a}}^{\mathrm{e}}, \tag{17}$$

directly in terms of its isochoric eigenvalues,

$$\tau_{i\mathrm{a}} = \frac{2\mu_i}{\alpha_i} \left[\frac{2}{3} (\tilde{\lambda}_{i\mathrm{a}}^{\mathrm{e}})^{\alpha_i} - \frac{1}{3} (\tilde{\lambda}_{i\mathrm{b}}^{\mathrm{e}})^{\alpha_i} - \frac{1}{3} (\tilde{\lambda}_{i\mathrm{c}}^{\mathrm{e}})^{\alpha_i} \right], \tag{18}$$

where $\mathrm{a}, \mathrm{b}, \mathrm{c} = \{1, 2, 3\}$ and $\mathrm{a} \neq \mathrm{b}, \mathrm{a} \neq \mathrm{c}$, and $\mathrm{b} \neq \mathrm{c}$. With the equilibrium stress $\boldsymbol{\tau}^{\mathrm{eq}}$ (15), the Kirchhoff stresses of each mode $\boldsymbol{\tau}_i$ (17) that

make up the non-equilibrium stress $\boldsymbol{\tau}^{\text{neq}}$ (13), and the Lagrange multiplier p, we can calculate the overall Piola stress,

$$\mathbf{P} = \frac{\partial \psi}{\partial \mathbf{F}} = \boldsymbol{\tau} \cdot \mathbf{F}^{-\text{t}} = [\boldsymbol{\tau}^{\text{eq}} + \boldsymbol{\tau}^{\text{neq}} - p\mathbf{I}] \cdot \mathbf{F}^{-\text{t}}. \tag{19}$$

It remains to specify the temporal evolution of the viscoelastic kinematics. Motivated by the reduced dissipation inequality for each mode [38], $\boldsymbol{\tau}_i : \mathbf{d}_i^{\text{v}} \geqslant 0$, and by the linear relation between hysteresis and maximum stress observed during our experiments in Fig. 3, we introduce the viscous stretch rates $\mathbf{d}_i^{\text{v}}$ as linear functions of the Kirchhoff stress $\boldsymbol{\tau}_i$ [39,36],

$$\mathbf{d}_i^{\text{v}} = \frac{1}{2\eta_i}\,\boldsymbol{\tau}_i. \tag{20}$$

Here η_i is the constant, deformation-independent viscosity and $\tau_i = \eta_i/\mu_i$ is the associated relaxation time near thermodynamic equilibrium. By reformulating the dissipation inequality in terms of the Lie derivative of the elastic left Cauchy-Green deformation tensor, $\mathcal{L}_v \mathbf{b}_i^{\text{e}} = -[2\mathbf{I}_i^{\text{v}} \cdot \mathbf{b}_i^{\text{e}}]^{\text{sym}}$, we obtain an evolution equation for the viscous stretch rate with a similar structure as in finite deformation elastoplasticity, $-\mathcal{L}_v \mathbf{b}_i^{\text{e}} \cdot (\mathbf{b}_i^{\text{e}})^{-1} = \boldsymbol{\tau}_i/\eta_i$ [40,31]. To advance the non-equilibrium part of the constitutive equations in time, we perform an implicit time integration with exponential update, see Appendix A.1 and Table A.8. For comparison, we also perform an explicit time integration, see Appendix A.2 and Table A.9.

3.4. Calibration of material parameters

Our viscoelastic model has $2 + 3m$ parameters, μ_∞ and α_∞ for the elastic part, and μ_i, α_i, and η_i for the $i = 1, .., m$ viscoelastic parts. To calibrate parameters for each brain region, we used the nonlinear least-squares algorithm *lsqnonlin* in MATLAB. We optimized two distinct parameter sets to best represent the average behavior during the first and third loading cycles. Material parameters calibrated with the first loading cycle characterize the unconditioned tissue response; parameters calibrated with the third loading cycle characterize the conditioned response and disregard the effects of fluid squeezed out during initial loading.

In both cases, we simultaneously considered all loading conditions for the calibration: simple shear, compression, and tension, as well as relaxation in shear and compression. We minimized the objective function,

$$\chi^2 = \sum_{i=1}^{n_{\text{s}}+n_{\text{rs}}} \left[P_{xz} - P_{xz}^{\psi}\right]_i^2 + \sum_{i=1}^{n_{\text{c}}+n_{\text{t}}+n_{\text{rc}}} \left[P_{zz} - P_{zz}^{\psi}\right]_i^2, \tag{21}$$

where $n_{\text{s}}, n_{\text{c}}, n_{\text{t}}, n_{\text{rs}}$, and n_{rc} are the numbers of experimental data points for shear, compression, tension, relaxation in shear, and relaxation in compression. For the relaxation experiments, we used smaller time increments and more data points during the loading phase than during the holding phase as indicated by the dots in Fig. 6d and e. In simple shear, the shear stresses P_{xz} and P_{yz} are independent of the Lagrange multiplier p. In unconfined compression and tension, we determine the Lagrange multiplier p in Eq. (19) from the lateral boundary conditions, $P_{xx} = P_{yy} \doteq 0$. Since the tissue behavior is history dependent, we have to evaluate the model for all three cycles when calibrating parameters for the third loading cycle. Yet, only the values of the third cycle entered the objective function (21). Since the shear modulus μ of the Ogden model (14) can only adopt positive values, we constrained it to $\mu > 0$.

To evaluate the goodness of fit, we determined the coefficient of determination, $R^2 = 1 - P^{\text{res}}/P^{\text{tot}}$, where $P^{\text{res}} = \sum_{i=1}^{n}(P_i - P_i^{\psi})^2$ is the sum of the squares of the residuals with the experimental data values P_i, the corresponding model data values P_i^{ψ}, and the number of data points n, and $P^{\text{tot}} = \sum_{i=1}^{n}(P_i - \bar{P})^2$ is the total sum of squares with the mean of the experimental data $\bar{P} = 1/n\sum_{i=1}^{n} P_i$. We used the R^2 values as indicators for the goodness of fit to highlight which of the five experiments would be best approximated by the data set of the simultaneous calibration with all five experiments.

4. Results

4.1. Pre-conditioning – General trends

Fig. 4a–c show the representative behavior during the first three cycles of simple shear, unconfined compression, and tension for a specimen from the corona radiata of brain *VIII*. Fig. 4d–f display the response predicted by our viscoelastic model with one mode, $m = 1$. In compression and tension, the model is capable of capturing the substantial pre-conditioning during the first loading cycle and the minor conditioning effects during all subsequent cycles. In simple shear, the model predictions deviate from the experimental data for the initial loading segment, but show good agreement for all subsequent cycles.

Fig. 5a shows the representative history-dependence during three loading cycles of compression at $\lambda = 0.9$ followed by three cycles of compression at $\lambda = 0.8$ for a specimen from the corona radiata of brain *VIII*. The sample displayed marked pre-conditioning during the first cycle of each load level associated with a pronounced softening. Fig. 5b demonstrates that our constitutive model accurately captures this characteristic history-dependence at different stretch levels. However, the model predicts larger residual stresses upon completing the first loading cycle of each stretch level than observed in the experiment.

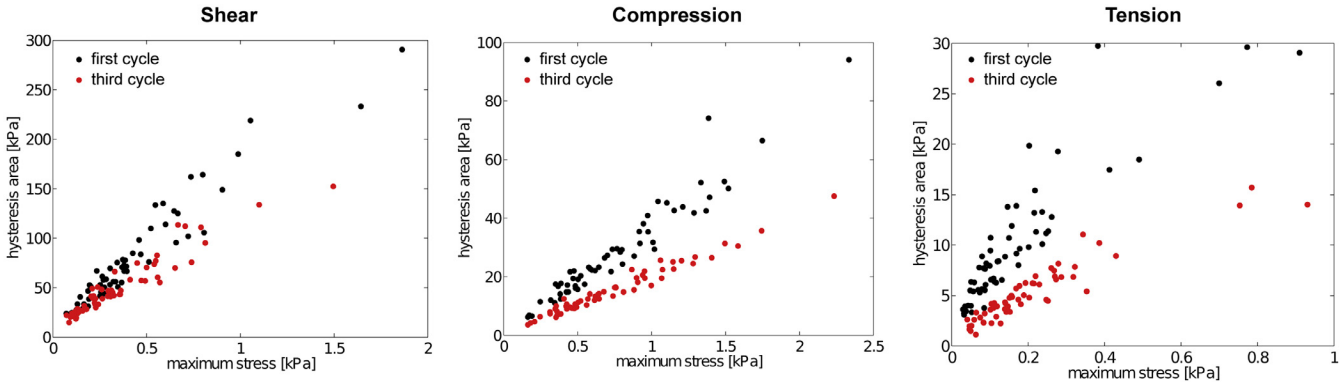

Fig. 3. Hysteresis versus maximum stress during the first and third loading cycles for all specimens tested in shear, compression, and tension. The data indicate that the dissipated energy increases linearly with the maximum recorded stress. This suggests a linear relation between the viscous stretch rate $\mathbf{d}_i^{\text{v}}$ and the Kirchhoff stress $\boldsymbol{\tau}_i$, thus $\mathbf{d}_i^{\text{v}} = \boldsymbol{\tau}_i/2\eta_i$. Hysteresis is larger for the first than for the third loading cycle.

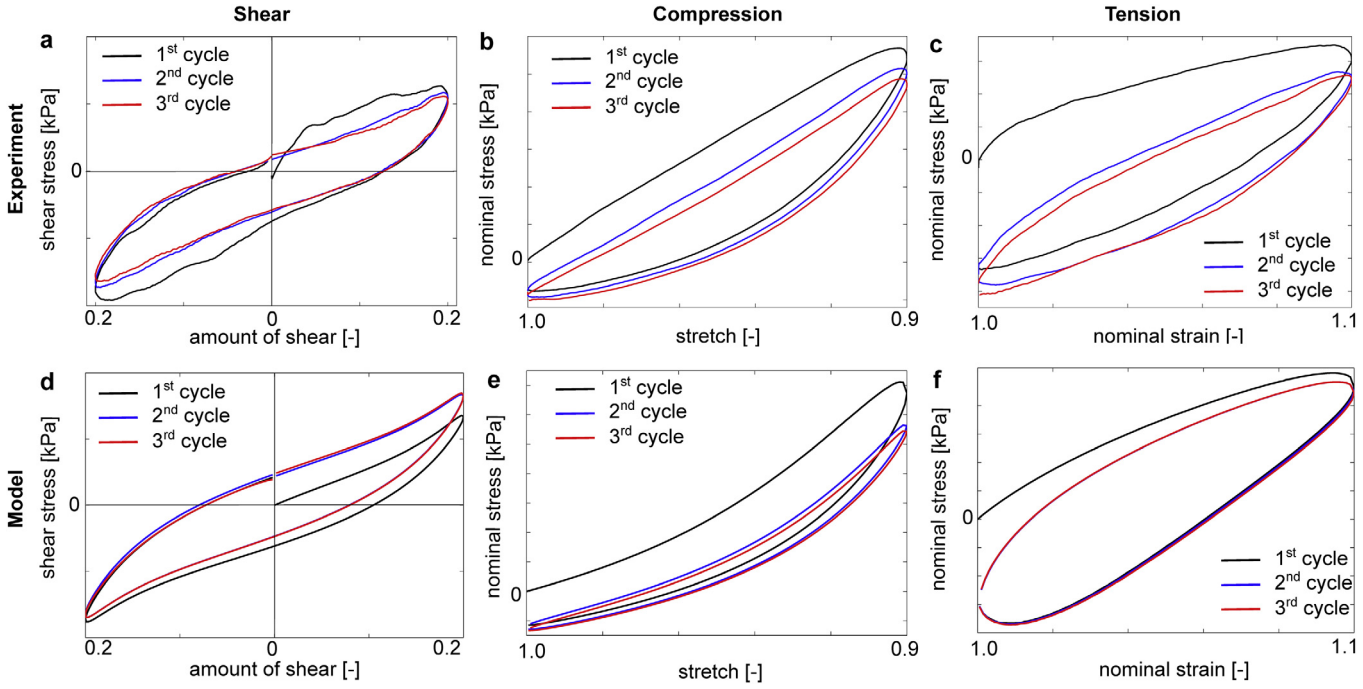

Fig. 4. Representative pre-conditioning behavior in shear, compression, and tension observed in the experiment for a specimen from the corona radiata of brain *VIII* (a-c), and predicted by the viscoelastic constitutive model (d-f). Both experiment and model reveal a substantial pre-conditioning during the first loading cycle. In compression and tension the qualitative behavior during cyclic loading agrees nicely. In simple shear, the model predicts lower shear stresses during the first cycle than during subsequent cycles, while the experiment shows the opposite behavior.

4.2. Unconditioned behavior - First loading cycle

Fig. 6 demonstrates that the viscoelastic constitutive model with one viscoelastic mode captures the general trends of the average unconditioned experimental data during the first cycle of simple shear, compression, tension, shear relaxation, and compression relaxation. Table 3 summarizes the corresponding material parameters for all brain regions, cortex, basal ganglia, corona radiata, and corpus callosum. The model with only one generalized Maxwell element underestimates the shear stresses, especially during the initial loading segment, and overestimates the stresses under tensile loading. Furthermore, it fails to capture the relaxation behavior over the entire holding time in Fig. 6d and e, which is also reflected in unrealistically high residual stresses at zero strain in the cyclic shear experiments in Fig. 6a. The coefficients of determination R^2 in Table 3 confirm these observations.

Fig. 7 shows that adding a second viscoelastic mode improves the agreement with the experimental data. With lower residual stresses at zero strain, the predictions for cyclic loading are now closer to the actual experimental data. In comparison to only one viscoelastic mode in Fig. 7c, the qualitative response in tension now agrees better with the experimental data. Table 4 summarizes the region-dependent material parameters. Larger coefficients of determination R^2 in Table 4 confirm the improved modeling of the experimental data.

Fig. 8 summarizes shear moduli and viscosities of the unconditioned tissue response in the different brain regions for the constitutive models with one and two generalized Maxwell elements. Independent of the number of viscoelastic modes, the equilibrium shear modulus μ_∞ is highest in the cortex, lowest in the corpus callosum, and comparable in basal ganglia and corpus callosum. The shear moduli for the viscoelastic modes are on average higher and reveal slightly different regional trends, depending on the corresponding viscosity. For large viscosities η_2, the cortex remains the stiffest region, but the stiffness for both white matter regions increases relative to both gray matter regions. For low viscosities η_1 in the first Maxwell element of the model with two viscoelastic modes, the corona radiata even has the largest shear modulus.

4.3. Conditioned behavior - Third loading cycle

Fig. 9 depicts the capability of the viscoelastic model with one viscoelastic mode to represent the average conditioned experimental data during the third cycle of simple shear, compression, tension, shear relaxation, and compression relaxation. Table 5 summarizes the corresponding material parameters for four regions of the brain, cortex, basal ganglia, corona radiata, and corpus callosum. The model captures the general features, but slightly underestimates the maximum stresses in simple shear and compression in Fig. 9a and b, and the hysteresis area in compression. It overestimates maximum tensile stresses in Fig. 9c for all the tested regions. Similar to the calibration with the first loading cycle in Section 4.2, one generalized Maxwell element is not sufficient to capture the relaxation behavior over the entire holding time in Fig. 9d and e.

Fig. 10 demonstrates that the constitutive model with two viscoelastic modes is able to achieve good agreement with the experimental data for all conducted modes and throughout the entire relaxation regime in Fig. 10d and e. Table 6 summarizes the corresponding region-dependent material parameters. The coefficients of determination R^2 in Table 4 indicate that, for tensile loading, the model displays the largest deviation from the experimental data.

Fig. 11 summarizes the shear moduli and viscosities of the conditioned tissue response in four brain regions for the constitutive models with one and two generalized Maxwell elements. Similar to the unconditioned response, the equilibrium shear modulus μ_∞ is highest in the cortex, lowest in the corpus callosum, and comparable in basal ganglia and corpus callosum. The same regional trends also apply to the shear modulus μ_2 in the Maxwell ele-

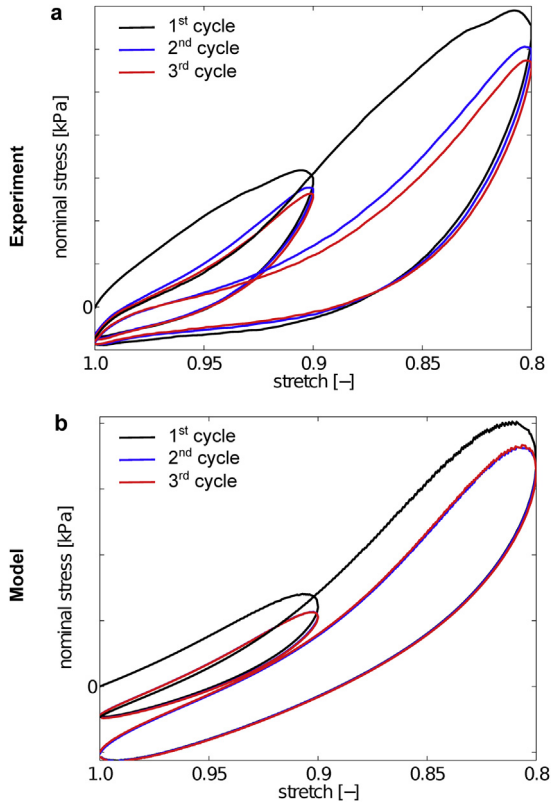

Fig. 5. Representative history-dependence for increasing compressive stretch with three cycles per stretch level. Nominal stress versus stretch behavior for a specimen from the corona radiata of brain *VIII*; experiment (a) and model prediction (b). At a stretch level of 0.9, the difference between the first and second cycles indicates pronounced pre-conditioning. When increasing the stretch level to 0.8, the first curve initially follows the pre-conditioned behavior up until 0.9; beyond 0.9, the curve again displays pronounced pre-conditioning between the first and second cycles. The model is capable of predicting this history-dependence at different load levels.

ment with higher viscosity η_2 for the model with two viscoelastic modes. The shear moduli μ_1 corresponding to lower viscosities η_1 are generally higher than μ_∞ and μ_2 and show slightly different regional trends: the cortex remains the stiffest region, but here basal ganglia and corpus callosum are softest, and the corona radiata lies in between. The lower viscosities η_1 show the same regional trends as the equilibrium shear moduli, while the higher viscosity η_2 is comparable in all four regions.

4.4. Characteristic time constants

Table 7 summarizes the characteristic time constants $\tau_i = \eta_i/\mu_i$ calculated from the material parameters in Tables 3–6. The model with a single viscoelastic mode fails to provide an accurate approximation of both early and late relaxation, and the corresponding time constants adopt intermediate values. For the unconditioned response, during the first loading cycle, the cortex responded slightly faster than the basal ganglia, and both responded faster than the white matter regions of the corona radiata and corpus callosum. For the conditioned response, during the third loading cycle, we observed the opposite trend; the corona radiata responded faster than the corpus callosum, and cortex and basal ganglia were equally slow. The time constants for the conditioned response were generally lower than for the unconditioned response.

The model with two viscoelastic modes seems sufficient to approximate the relaxation behavior over the entire holding time. When considering the fast time constant τ_1, the basal ganglia responded slowest, and corona radiata and corpus callosum fastest. For the third cycle, white matter displayed on average longer relaxation times than gray matter with higher time constants τ_2. While the short time scales were only slightly larger for the conditioned response than for the unconditioned response, there was a remarkable difference in the long time scales, which were much larger for the third cycle.

5. Discussion

Computational simulations have become a powerful tool to understand the human brain, protect it against injuries, and improve neurosurgical procedures. The value of a computational prediction critically depends on the choice of the constitutive model that characterizes the underlying tissue rheology. For the brain-unlike for most soft tissues-this is exceptionally challenging, because the rheology of the brain is highly sensitive to loading conditions and time scales. In this study, we have established a rheological model for human brain tissue that captures the nonlinear, time-dependent behavior of different brain regions under multiple loading conditions in a finite strain setting. Our objective was to identify a model that simultaneously captures a variety of loading scenarios with a limited number of well-defined parameters. To calibrate the model, we performed five different tests: simple shear, unconfined compression, tension, shear relaxation, and compression relaxation. Since brain tissue is highly heterogeneous, we performed the series of all five tests on one and the same sample to avoid inter-specimen variations.

5.1. Finite viscoelasticity captures nonlinear, time-dependent behavior

We chose a class of models based on the multiplicative decomposition of the deformation gradient into elastic and viscous parts, $\mathbf{F} = \mathbf{F}_i^e \cdot \mathbf{F}_i^v$ [30,29], and the additive decomposition of the free energy into equilibrium and non-equilibrium parts, $\psi = \psi^{eq} + \psi^{neq}$, in terms of $i = 1,..,m$ parallel viscoelastic modes [41,42]. Within this framework, we represent history-dependence through the viscous right Cauchy-Green deformation tensors, $\mathbf{C}_i^v$, or rather their inverses, $(\mathbf{C}_i^v)^{-1}$, which we introduce as internal variables. To advance these internal variables in time, we adopt an implicit time integration scheme based on an operator split [38] with exponential update [32], Appendix A.1. For comparison, we also implemented an explicit time integration scheme as proposed in previous studies of porcine brain under shear [17] and unconfined compression [18], Appendix A.2. In contrast to the classical Prony series approach [8,26,43], our finite viscoelasticity approach uses the entire loading history-including the loading ramp-instead of assuming instantaneous loading [32,38]. As a result, it naturally provides additional information about the elastic parameters during loading and is less sensitive to the selection of data points used for the fit [29].

5.2. Simultaneous parameter identification for five loading modes yields generic viscoelastic parameters

Previous studies focus on a single mode of loading, shear [20], compression [44], or tension [43], which implies that they neglect the pronounced tension-compression asymmetry of brain tissue [8,9]. Here we simultaneously calibrated five different modes of loading-shear, compression, tension, shear relaxation, and compression relaxation-using a modified one-term Ogden model with two parameters, the shear modulus μ and the tension-compression asymmetry α [37]. In a systematic comparison, recent studies have shown that the Ogden model outperforms

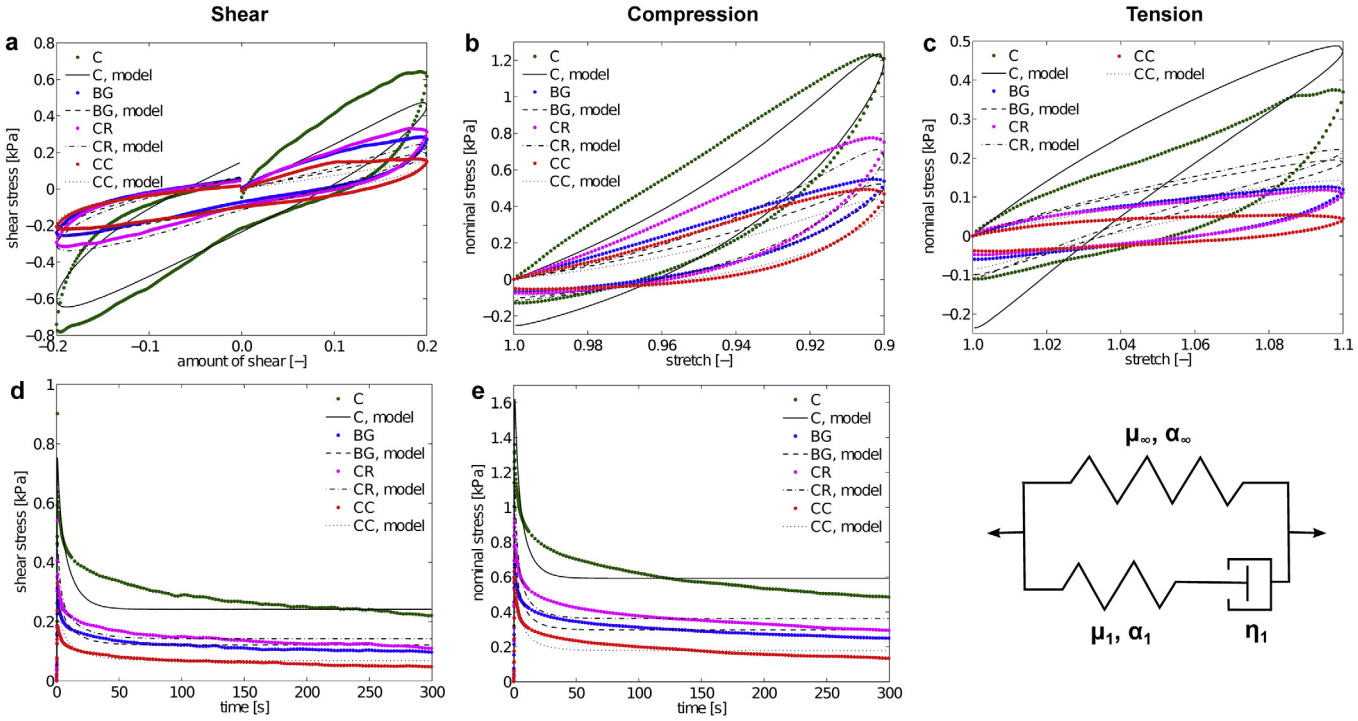

Fig. 6. Average experimental data during the **first** loading cycle in four regions, cortex (C, $n = 13$), basal ganglia (BG, $n = 15$), corona radiata (CR, $n = 19$), and corpus callosum (CC, $n = 11$), and corresponding constitutive model with **one** viscoelastic mode. We obtained one set of constitutive parameters for each region by simultaneously calibrating the model for all five tests, simple shear (a), compression (b), tension (c), shear relaxation (d), and compression relaxation (e), see Table 3.

Table 3
Constitutive parameters and coefficients of determination for the viscoelastic model with one Maxwell element, calibrated simultaneously for the averaged **first** loading cycles of shear, compression, tension, shear relaxation, and compression relaxation in four regions, corpus callosum (CC), corona radiata (CR), basal ganglia (BG), and cortex (C), see Fig. 6.

first cycle	μ_∞ [kPa]	α_∞ [–]	μ_1 [kPa]	α_1 [–]	η_1 [kPa·s]	R^2_s [–]	R^2_c [–]	R^2_t [–]	R^2_{rs} [–]	R^2_{rc} [–]
C	0.65	-20.75	2.07	-13.55	20.05	0.941	0.943	0.361	0.876	0.819
BG	0.32	-20.71	0.79	-15.99	9.87	0.911	0.934	0.185	0.865	0.868
CR	0.29	-25.39	0.91	-23.41	13.51	0.929	0.911	0.000	0.853	0.817
CC	0.11	-29.34	0.70	-23.14	10.47	0.940	0.894	0.000	0.630	0.839

other popular constitutive models for brain tissues including the neo-Hookean model, the Mooney Rivlin model, the Demiray model, and the Gent model [10,45]. Here we adopted the Ogden model for both, the equilibrium part ψ^{eq} and the non-equilibrium part ψ^{neq} of the viscoelastic model, and compared formulations with $m = 1$ viscous modes in Figs. 6 and 9 and $m = 2$ viscous modes in Figs. 7 and 10. Our parameter identification was stable and robust for all four cases in Tables 3–6, and the algorithm reproducibly identified the same local minimum of the objective function (21) for different sets of initial values. As indicated by the coefficients of determination, all four models perform well under shear and compression, both in quasi-static loading and under stress relaxation, but perform poorly under tension. The literature has long acknowledged that brain tissue behaves differently in tension and compression [8]. This is in agreement with several recent studies that recognize the challenges of finding a single constitutive model for brain tissue under different types of loading [45,46]. We are currently in the process of designing a family of hyperelastic models for human brain tissue under multiple loading modes to better address these limitations [47]. This study clearly highlights the need and potential for further investigation.

5.3. Two-parameter Ogden model captures tension-compression asymmetry

Our family of viscoelastic models-the elastic Ogden model combined with the viscous Ogden model with $m = 1$ and $m = 2$ viscous modes-captures the experimentally observed tension-compression asymmetry. Rather than explicitly introducing different stiffnesses in tension and compression, the modified Ogden model inherently represents tension-compression asymmetry through the model parameter α [10]. Several studies have successfully adopted Ogden type models for brain tissue [8,43,45], an approach we have decided to follow here. While we have improved the parameterization compared to previous models based on a single loading mode [16–18], the asymmetry predicted by our model still remains less pronounced than observed in our experiments. To improve the fit of the model-especially under tensile loading-we could explicitly discriminate between compression and tension and introduce different parameter sets for different loading modes [10]. However, switching between different parameter sets would make the model less suitable for physiological mixed-mode loading, and, ultimately, for finite element simulations of surgical procedures [2,48]. The major objective of the current study was therefore to

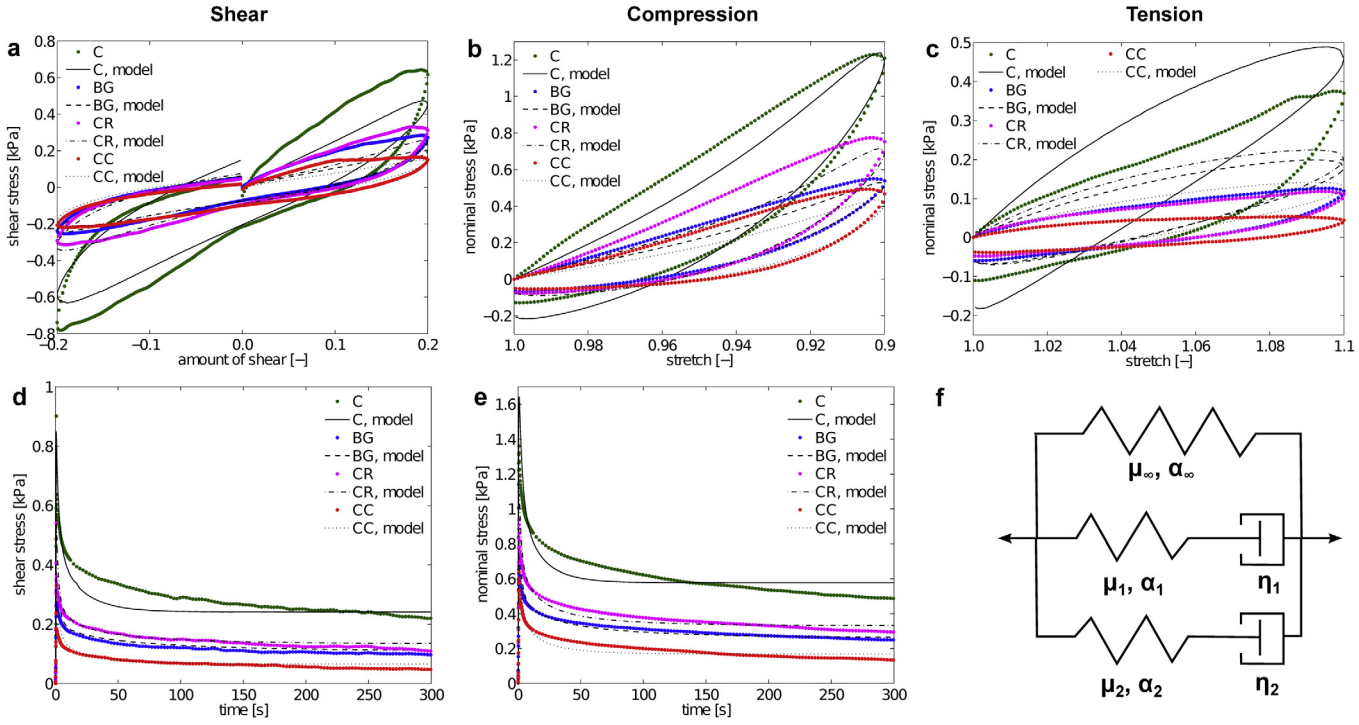

Fig. 7. Average experimental data during the **first** loading cycle in four regions, cortex (C, $n = 13$), basal ganglia (BG, $n = 15$), corona radiata (CR, $n = 19$), and corpus callosum (CC, $n = 11$), and corresponding constitutive model with **two** viscoelastic modes. We obtained one set of constitutive parameters for each region by simultaneously calibrating the model for all five tests, simple shear (a), compression (b), tension (c), shear relaxation (d), and compression relaxation (e), see Table 4.

Table 4
Constitutive parameters and coefficients of determination for the viscoelastic model with **two** Maxwell elements, calibrated simultaneously for the averaged **first** loading cycles of shear, compression, tension, shear relaxation, and compression relaxation in four regions, corpus callosum (CC), corona radiata (CR), basal ganglia (BG), and cortex (C), see Fig. 7.

first cycle	μ_∞ [kPa]	α_∞ [–]	μ_1 [kPa]	α_1 [–]	η_1 [kPa·s]	μ_2 [kPa]	α_2 [–]	η_2 [kPa·s]	R^2_s [–]	R^2_c [–]	R^2_t [–]	R^2_{rs} [–]	R^2_{rc} [–]
C	0.74	-18.01	1.46	6.71	2.38	1.28	-15.46	24.74	0.936	0.956	0.448	0.892	0.827
BG	0.34	-17.99	1.01	2.12	2.39	0.33	-17.21	32.51	0.922	0.950	0.321	0.848	0.920
CR	0.35	-21.10	1.60	3.25	2.03	0.46	-22.47	28.04	0.945	0.926	0.000	0.850	0.894
CC	0.13	-26.45	0.91	1.52	1.15	0.45	-21.11	14.23	0.925	0.904	0.000	0.627	0.885

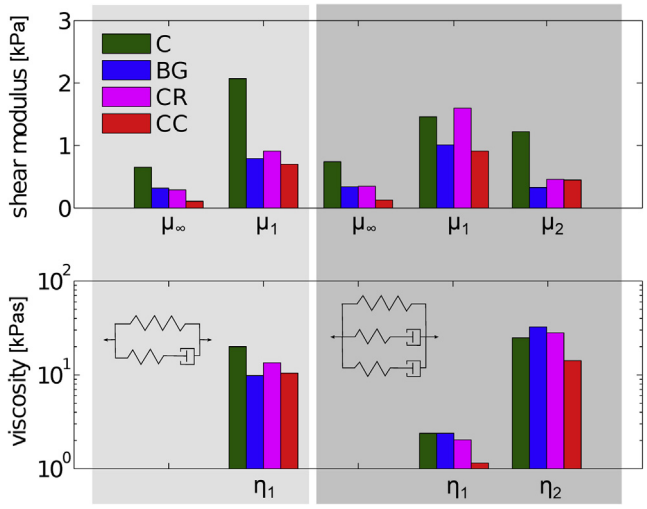

Fig. 8. Shear moduli and viscosities during the **first** loading cycle for four regions, cortex (C), basal ganglia (BG), corona radiata (CR), and corpus callosum (CC), with **one** (left) and **two** (right) generalized Maxwell modes.

characterize brain tissue through a single, simple constitutive model with a limited number of well-defined material parameters. The simplest model of our family is the finite viscoelastic model with one viscous mode in Fig. 6 and five material parameters in Table 3. Its elastic and viscous shear stiffnesses varied between $\mu_\infty = 0.65$ kPa and $\mu_1 = 2.07$ kPa in the gray matter of the cortex and $\mu_\infty = 0.29$ kPa and $\mu_1 = 0.91$ kPa in the white matter of the corona radiata. In all regions, the asymmetry parameters α_∞ and α_1 were negative and on the order of $\alpha \approx -20$ and the characteristic time constant η_1 was on the order of $\eta_1 \approx 10 - 20$ s. Compared to our previous purely hyperelastic modified one-term Ogden model [10], in all four regions, the elastic shear moduli μ_∞ of the viscoelastic model were about half the size of the shear moduli μ of the purely elastic model, while asymmetry parameters α_∞ and α took similar values.

5.4. Constant-viscosity model captures pre-conditioning and hysteresis

Our experiments reveal two general trends: Brain tissue displays a unique pre-conditioning behavior, see Fig. 4, and its hysteresis increases linearly with the maximum recorded stress, see Fig. 3. To capture these characteristics while keeping the constitu-

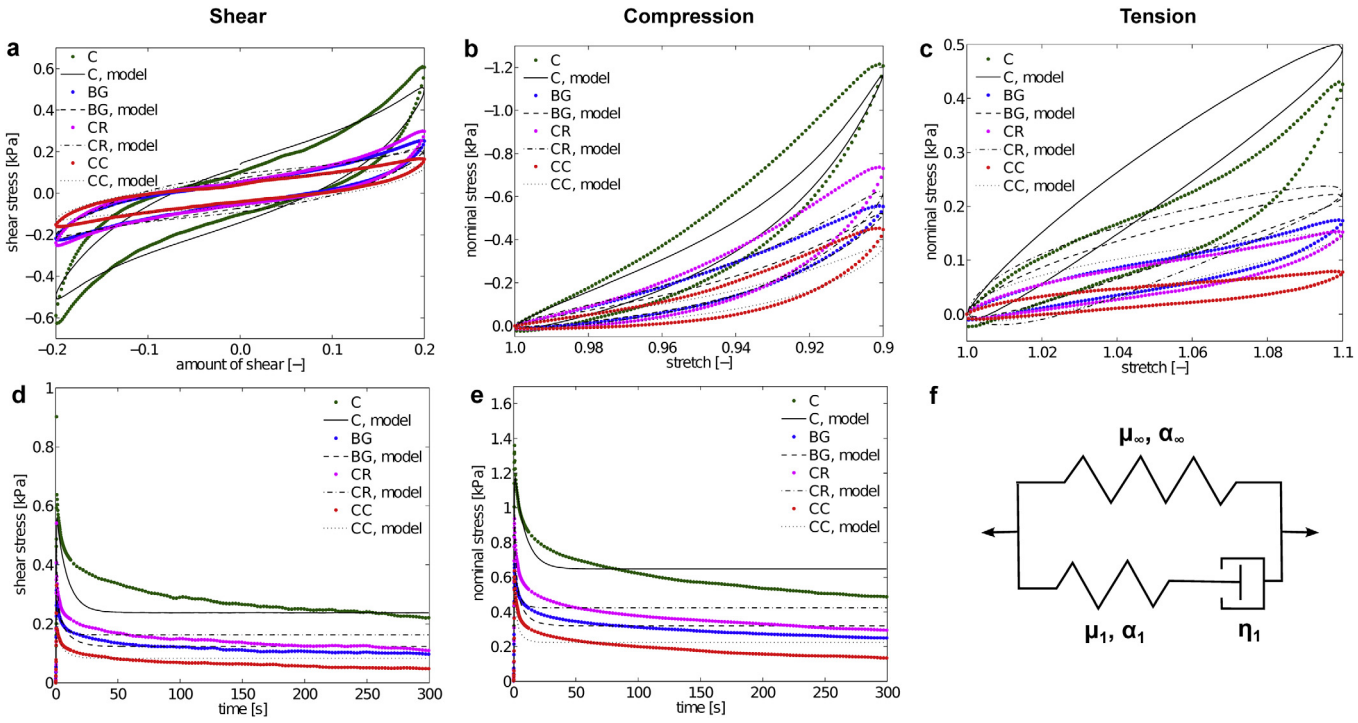

Fig. 9. Average experimental data during the **third** loading cycle in four regions, cortex (C, $n = 13$), basal ganglia (BG, $n = 15$), corona radiata (CR, $n = 19$), and corpus callosum (CC, $n = 11$), and corresponding constitutive model with **one** viscoelastic mode. We obtained one set of constitutive parameters for each region by simultaneously calibrating the model for all five tests, simple shear (a), compression (b), tension (c), shear relaxation (d), and compression relaxation (e), see Table 5.

Table 5
Constitutive parameters and coefficients of determination for the viscoelastic model with **one** Maxwell element, calibrated simultaneously for the averaged **third** loading cycles of shear, compression, tension, shear relaxation, and compression relaxation in four regions, corpus callosum (CC), corona radiata (CR), basal ganglia (BG), and cortex (C), see Fig. 9.

third cycle	μ_∞ [kPa]	α_∞ [–]	μ_1 [kPa]	α_1 [–]	η_1 [kPa·s]	R^2_s [–]	R^2_c [–]	R^2_t [–]	R^2_{rs} [–]	R^2_{rc} [–]
C	0.24	-35.83	1.69	-0.01	14.64	0.864	0.798	0.000	0.753	0.797
BG	0.20	-29.15	0.71	-11.77	6.19	0.934	0.848	0.000	0.847	0.832
CR	0.25	-29.62	0.91	-25.11	3.87	0.868	0.811	0.000	0.806	0.688
CC	0.09	-35.06	0.56	-27.19	3.37	0.793	0.707	0.000	0.756	0.739

tive model as simple as possible, we assumed a linear relation between the viscous stretch rate $\mathbf{d}_i^v$ and the Kirchhoff stress $\boldsymbol{\tau}_i$ [32,39], and introduced a single constant viscosity parameter η_i for each viscoelastic mode. In the small strain limit, this implies that each viscoelastic mode reduces to a generalized Maxwell element with an elastic spring [32]. While several more advanced models propose a non-constant viscosity parameter to brain deformation as a non-Newtonian flow in a porous medium [16,17], e.g., using the Ellis model, $\eta = \eta_\infty + [\eta_0 - \eta_\infty]/[1 + [\tau/\tau_0]^{n-1}]$, here we adopt a constant-viscosity approach. This assumption agrees with recent biaxial extension tests [27] and unconfined compression tests [18] on porcine brain.

5.5. Two-time-constant model captures early and late relaxation

Our study shows that a viscoelastic model with only one viscoelastic mode, with four elastic parameters $\mu_\infty, \alpha_\infty, \mu_1$ and α_1 and one characteristic time constant $\tau_1 = \eta_1/\mu_1$, captures the main features of brain tissue under shear, compression, and tension, but is not capable of reproducing both the early and late relaxation behavior, see Figs. 6 and 9. The model with two viscoelastic modes, with six elastic parameters and two characteristic time constants, performed well across the entire relaxation regime both under shear and compression, see Figs. 7 and 10. This agrees well with several studies, which suggest that two time constants were sufficient to accurately represent stress relaxation [20,23,26,48,49], whereas a few other studies favor a three-time-constant approach [15,50,51].

5.6. Monophasic model captures viscous but not porous effects

Our viscoelastic model successfully characterizes the effects of pre-conditioning during the first loading cycle in compression and tension, and the reduced conditioning effects during all subsequent cycles, see Fig. 4. It also predicts the successive softening when increasing the strain in a step-wise fashion, see Fig. 5. For simple shear, the model predictions agree well with the experimental behavior during the second and third cycles; for the initial loading segment, however, the predicted stresses are lower than during subsequent cycles, which is opposite to our experimental observations. This difference is likely caused by the pore fluid that squeezes out of the sample when it is first loaded [9]. Our

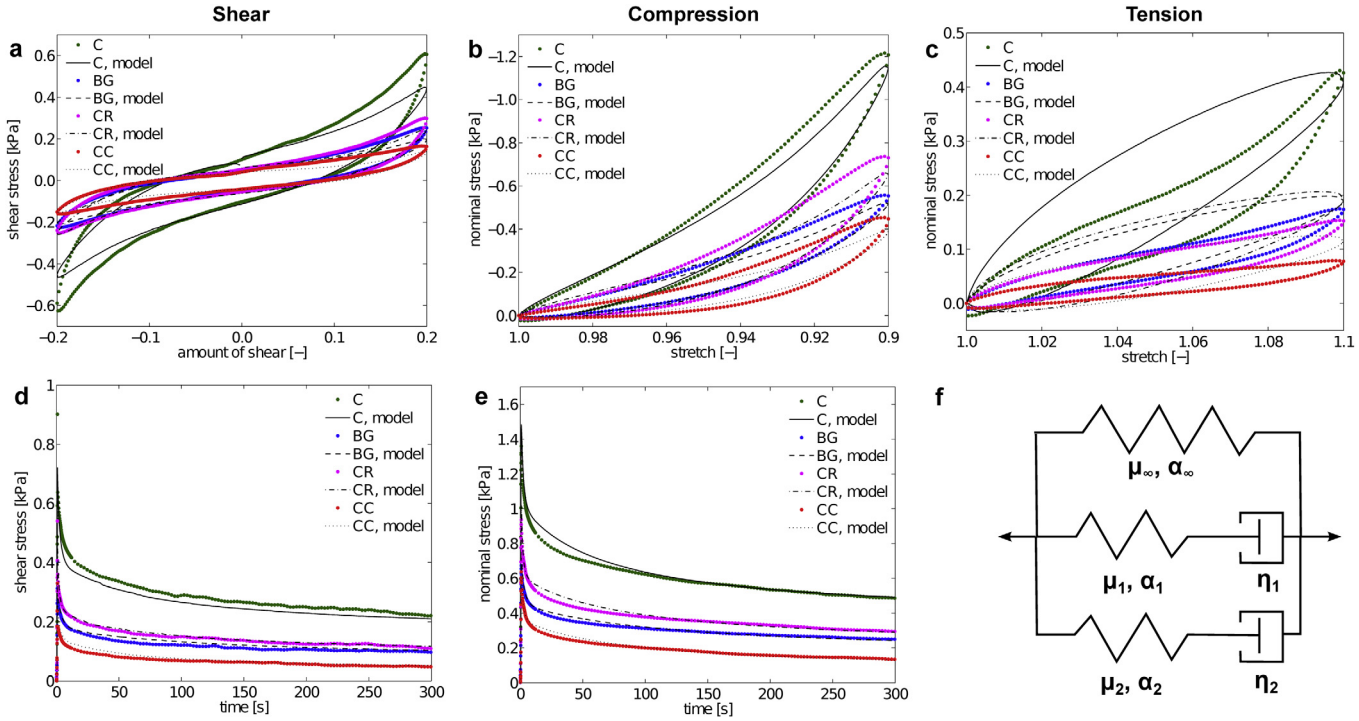

Fig. 10. Average experimental data during the **third** loading cycle in four regions, cortex (C, $n = 13$), basal ganglia (BG, $n = 15$), corona radiata (CR, $n = 19$), and corpus callosum (CC, $n = 11$), and corresponding constitutive model with **two** viscoelastic modes. We obtained one set of constitutive parameters for each region by simultaneously calibrating the model for all five tests, simple shear (a), compression (b), tension (c), shear relaxation (d), and compression relaxation (e), see Table 6.

Table 6
Constitutive parameters and coefficients of determination for the viscoelastic model with **two** Maxwell elements, calibrated simultaneously for the averaged **third** loading cycles of shear, compression, tension, shear relaxation, and compression relaxation in four regions, corpus callosum (CC), corona radiata (CR), basal ganglia (BG), and cortex (C), see Fig. 10.

third cycle	μ_∞ [kPa]	α_∞ [–]	μ_1 [kPa]	α_1 [–]	η_1 [kPa·s]	μ_2 [kPa]	α_2 [–]	η_2 [kPa·s]	R_s^2 [–]	R_c^2 [–]	R_t^2 [–]	R_{rs}^2 [–]	R_{rc}^2 [–]
C	0.42	-21.27	1.40	-14.66	3.05	0.56	-23.76	289.37	0.798	0.880	0.500	0.928	0.956
BG	0.17	-21.52	0.68	-15.50	2.27	0.27	-22.76	240.17	0.890	0.901	0.000	0.931	0.956
CR	0.16	-25.66	0.97	-25.35	2.19	0.25	-29.22	299.79	0.862	0.832	0.000	0.965	0.944
CC	0.04	-28.41	0.63	-27.01	1.62	0.16	-30.80	232.53	0.747	0.763	0.000	0.853	0.971

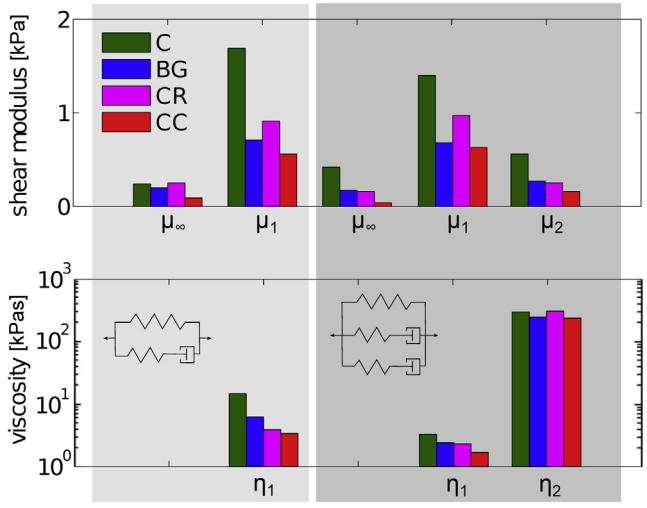

Fig. 11. Shear moduli and viscosities during the **third** loading cycle for four regions, cortex (C), basal ganglia (BG), corona radiata (CR), and corpus callosum (CC), with **one** (left) and **two** (right) generalized Maxwell modes.

Table 7
Characteristic time constants $\tau_i = \eta_i/\mu_i$ near thermodynamic equilibrium for **one** and **two** generalized Maxwell modes from calibrating the constitutive model with the **first** and **third** loading cycles.

	first cycle			third cycle		
	τ_1 [s]	τ_1 [s]	τ_2 [s]	τ_1 [s]	τ_1 [s]	τ_2 [s]
C	9.69	1.63	20.28	8.66	2.18	516.73
BG	12.49	2.37	98.52	8.72	3.34	889.52
CR	14.85	1.27	60.96	4.25	2.26	1199.16
CC	14.96	1.26	31.62	6.02	2.57	1453.31

monophasic viscoelastic model can only implicitly capture these porous effects [52]. To accurately model the fluid flow within the tissue, we could use a biphasic poro-viscoelastic model [1,53,54]. While this is beyond the scope of our current study, we will address this aspect in the future to contrast and compare viscous and porous effects in human brain tissue.

5.7. Unconditioned tissue is stiffer than pre-conditioned tissue

Our experiments confirm that the rheology of ultra-soft tissues like the human brain is highly sensitive to the loading history. To quantify this effect, we calibrated the model for two separate parameter sets, for the unconditioned response using the first loading cycle in Fig. 8 and for the conditioned response using the third loading cycle in Fig. 11. Strikingly, the unconditioned tissue was markedly stiffer than the conditioned tissue in all four brain regions. While the gray matter stiffness of the cortex varied by almost a factor three between 0.65 kPa and 0.24 kPa, the white matter stiffness of the corona radiata varied only marginally between 0.29 kPa and 0.25 kPa. We would like to point out though that there is no 'right' or 'wrong' set of parameters: Depending on the application of interest-for example the interpretation of an *ex vivo* test or the prediction of an *in vivo* response-either the unconditioned or conditioned data could become relevant. Notably, the conditioned response displayed larger slow time constants than the unconditioned response, although we calibrated both parameter sets in Table 7 with exactly the same stress relaxation experiments. This indicates that the cyclic experiments have a pronounced effect on the viscoelastic parameter identification. Comparing the unconditioned and conditioned behavior suggests that we can attribute the shorter time scale, τ_1, to the viscous component of the solid phase and the longer time scale, τ_2, to porous effects of the fluid phase. When using the conditioned response of the third cycle for our calibration, we intentionally neglect this porous effect and, accordingly, the slow time constant adopts significantly larger values. This agrees well with a previous study that reported a pre-conditioned viscosity of 60 kPas in unconfined compression tests of porcine brain [18]. Our observations help to better understand the individual time-dependent contributions of the solid and fluid phases [9], which become especially important when we attempt to interpret and model brain tissue as a biphasic material [15,53,54].

5.8. Unconfined gray matter is stiffer than white matter

Our study reveals significant regional differences in stiffness, where the cortex is generally the stiffest region, followed by the basal ganglia and the corona radiata, and, last, by the corpus callosum. However, these general trends are sensitive to the corresponding time scales. When time scales become shorter, white matter regions tend to stiffen relative to gray matter regions. At the lowest time scales, for the unconditioned response of the model with two viscoelastic modes in Table 4, the corona radiata becomes the stiffest region. The relative stiffening of white matter compared to gray matter at decreasing time scales is more pronounced for the unconditioned than for the conditioned response, which suggests that this effect is at least partially associated with the fluid phase. This could explain why indentation experiments with relatively large indenters record larger stiffnesses for white matter than for gray matter [22,23,25,55]: During confined compression, the fluid cannot escape quickly and the experiment probes both solid and fluid phases. When the indenter is small enough to only probe the solid phase, we observe the opposite trend with larger stiffnesses in gray than in white matter [21,56], which agrees well with the present study.

5.9. Limitations

Our rheological characterization of human brain tissue has several natural limitations: First, by the very nature of triaxial testing, gluing the sample to the specimen holder may induce boundary effects and the deformation might not be as homogeneous as we had assumed. Similarly, gravity effects that deform the initially cubic samples induce additional heterogeneities and possibly also pre-conditioning. While submerged conditions could possibly reduce these effects, testing the sample within a bath might introduce other limitations associated with fluid-uptake and swelling [34]. We are currently considering a combination of drained and un-drained experiments [9] to reduce these limitations and characterize brain as a poro-viscoelastic solid.

Second, with a maximum shear of $\gamma = 0.2$ and stretches of $\lambda = 0.9$ and $\lambda = 1.1$, our samples might have experienced some degree of tissue damage [9]. While we have previously shown that our specimens fully recover within a recovery period of one hour for compression levels of $\lambda = 0.9$ [10], reported strain injury thresholds range from $\gamma = 0.16$ in shear [57] to $\lambda = 1.21$ in tension [58]. However, for small deformations that lie safely within this regime, we found that the recording accuracy becomes a limitation for all loading modes. This could also explain why the residual stresses upon completion of the first loading cycle were larger in the model than in the experiments. Although it remains unclear whether brain tissue truly experiences shear and stretch beyond this regime under physiological conditions *in vivo*, we are currently conducting combined compression/tension-shear tests to validate the proposed model for larger shear and stretch levels and quantify potential tissue damage.

Third, because of the ultra-soft nature of brain tissue, our recorded tensile forces were extremely small and sometimes close to the sensitivity of our force sensors. The challenges of probing brain tissue in tension are well acknowledged in the literature [8,43]. In the low-force regime, our tensile tests-and with them the tensile fit-are therefore less accurate than the shear and compression fit. For similar reasons, we could not perform reasonable relaxation tests in tension, which might explain a calibration bias towards shear and compression, which were much better reproduced by the model than tension.

Fourth, we only considered quasi-static and stress relaxation experiments to calibrate our model in the slow-to-moderate loading regime. We loaded all specimens at the same speed; since the dimensions of the specimens may vary, in retrospect, it would have been more consistent to adjust the speed and load all specimens at the same strain rate. Limited by the capabilities of our testing device, we were not able to probe the tissue at extreme loading rates. Our study was intentionally designed to understand the brain under physiological conditions. This implies that our model parameters are well suited to model phenomena of neurodevelopment [59] and neurosurgery [2]; yet, it is likely that our results will not directly translate into the extremely fast loading regime to model phenomena of traumatic brain injury.

Last, and maybe most importantly, an evident limitation of our study is that it is based on non-living, isolated human brain samples. Undoubtedly, the *ex vivo* response under simple shear, unconfined compression, and extension is different from the behavior of the living brain under complex mixed loading conditions *in vivo* [60,61], and further studies are needed to establish correlations between brain tissue *ex vivo* and *in vivo*. With rapid developments in magnetic resonance elastography [62], we are beginning to gain a deeper insight into the complex rheology of the human *in vivo* [63]. While magnetic resonance elastography is a promising technology to non-invasively characterize the loss and storage moduli of the living brain, it is usually associated with the assumptions of linear elasticity, isotropy, homogeneity, and incompressibility [64]. We are currently performing combined magnetic resonance elastography, tissue histology, and mechanical testing [65] to cross-validate these methods for porcine brains. Along those lines, the regional data of the current study could provide valuable information to calibrate and validate magnetic resonance elastography for human brains.

6. Conclusion

We have characterized the rheology of human brain tissue through a family of finite viscoelastic Ogden-type models and successfully identified their parameters for multiple loading modes in four different regions of the brain. Our viscoelastic brain models are straightforward to integrate-if not already present-in standard nonlinear finite element solvers. Even the simplest model of the family, with only one viscoelastic mode and five material parameters, naturally captures the essential features of brain tissue: its characteristic nonlinearity, pre-conditioning, hysteresis, and tension-compression asymmetry. For the first time, we have simultaneously identified a single parameter set for shear, compression, tension, shear relaxation, and compression relaxation loading. This parameter set is critical for computational simulations under physiological conditions, where loading is naturally of mixed mode nature. Especially in regions of gray matter, we observed a marked sensitivity to pre-conditioning. This suggests that in certain brain regions, at certain loading rates, additional time-dependent effects like poroelasticity could play a non-negligible role. Understanding the characteristic rheology of the human brain will improve simulations of human brain development and neurosurgical procedures with the ultimate goal to enhance personalized treatment planning.

Acknowledgements

This study was supported by the German National Science Foundation Grant STE 544/50 to SB and PS, and by the Humboldt Research Award to EK.

Appendix A. Time integration

A.1. Implicit exponential time integration

In this study, we adopt an implicit exponential time integration scheme to advance the viscoelastic constitutive equations in time [31,32,38]. We divide the testing period of interest into discrete time intervals $t \in [t_n, t]$ with $\Delta t = t - t_n \geqslant 0$, where we denote all quantities of the previous time step through the subscript $(\circ)_n$ and neglect the subscript $(\circ)_{n+1}$ for all current quantities for notational simplicity. From the experiments, we know the deformation gradient $\mathbf{F}$ of the current time step t. From the discrete time integration, we know the internal variables, the inverse viscous right Cauchy-Green deformation tensors $(\mathbf{C}^v_{i,n})^{-1}$ of all i modes, of the previous time step t_n. Prior to the first time step, we initialize all internal variables to the unit tensor, $(\mathbf{C}^v_{i,0})^{-1} = \mathbf{I}$. Central to the implicit time integration is the evolution equation for the elastic right Cauchy-Green deformation tensor,

$$\dot{\mathbf{b}}^e_i = \mathbf{F} \cdot (\dot{\mathbf{C}}^v_i)^{-1} \cdot \mathbf{F}^t + \dot{\mathbf{F}} \cdot (\mathbf{C}^v_i)^{-1} \cdot \mathbf{F}^t + \mathbf{F} \cdot (\mathbf{C}^v_i)^{-1} \cdot \dot{\mathbf{F}}^t. \tag{A.1}$$

We integrate this evolution equation implicitly using an exponential mapping algorithm [40,31] based on an operator split with an elastic predictor and an iterative inelastic corrector step. In the *elastic predictor step*, indicated by the subscript $[\circ]_{tr}$, we freeze the inelastic deformation, $(\mathbf{C}^v_i)^{-1} = (\mathbf{C}^v_{i,n})^{-1}$, and determine the trial elastic Cauchy-Green deformation tensors using Eq. (8),

$$[\mathbf{b}^e_i]_{tr} = \mathbf{F} \cdot (\mathbf{C}^v_i)^{-1}_n \cdot \mathbf{F}^t. \tag{A.2}$$

From their spectral representation,

$$[\mathbf{b}^e_i]_{tr} = \sum_{a=1}^{3} [\lambda^e_{ia}]^2_{tr} \, [\mathbf{n}^e_{ia}]_{tr} \otimes [\mathbf{n}^e_{ia}]_{tr}. \tag{A.3}$$

we calculate the trial elastic eigenvalues $[\lambda^e_{ia}]_{tr}$. In the *inelastic corrector step*, we evaluate the rate of the elastic Cauchy-Green deformation tensors using Eq. (A.1), but now freeze the spatial velocity gradient, $\mathbf{l} = 0$, and thus, $\dot{\mathbf{F}} = 0$, which only leaves a single term, $\dot{\mathbf{b}}^e_i = \mathbf{F} \cdot (\dot{\mathbf{C}}^v_i)^{-1} \cdot \mathbf{F}^t = \mathcal{L}_v \mathbf{b}^e_i$. During the corrector step, this term is equivalent to the Lie-derivative, $\mathcal{L}_v \mathbf{b}^e_i$, of the elastic left Cauchy-Green deformation tensor along the velocity field of the material motion. We reformulate the evolution Eq. (20) in terms of the Lie derivative, $\boldsymbol{\tau}_i / \eta_i = -\mathcal{L}_v \mathbf{b}^e_i \cdot (\mathbf{b}^e_i)^{-1}$, to express the rate of the elastic Cauchy-Green deformation tensors [31],

$$\dot{\mathbf{b}}^e_i = -\frac{1}{\eta_i} \boldsymbol{\tau}_i \cdot \mathbf{b}^e_i. \tag{A.4}$$

We approximate Eq. (A.4) using an exponential map with the initial value $[\mathbf{b}^e_i]_{tr}$ from Eq. (A.2)[38,32],

$$\mathbf{b}^e_i = \exp\left(-\frac{\Delta t}{\eta_i} \boldsymbol{\tau}_i\right) [\mathbf{b}^e_i]_{tr}. \tag{A.5}$$

In the case of material isotropy, $\boldsymbol{\tau}_i$ and $\mathbf{b}^e_i$ share the same eigenvectors, $[\mathbf{b}^e_i]_{tr}$ is coaxial to $\mathbf{b}^e_i$ with $[\mathbf{n}^e_{ia}]_{tr} = \mathbf{n}^e_{ia}$, and we can write Eq. (A.5) in the eigenspace and express it in terms of the elastic stretches λ^e_{ia} and elastic trial stretches $[\lambda^e_{ia}]_{tr}$,

$$(\lambda^e_{ia})^2 = \exp\left(-\frac{\Delta t}{\eta_i} \tau_{ia}\right) [\lambda^e_{ia}]^2_{tr}. \tag{A.6}$$

Taking the logarithm of both sides, we obtain a nonlinear equation for the elastic logarithmic principal stretches ϵ^e_{ia},

$$\epsilon^e_{ia} = \ln(\lambda^e_{ia}) = -\frac{\Delta t}{2\eta_i} \tau_{ia} + [\epsilon^e_{ia}]_{tr}. \tag{A.7}$$

To iteratively solve Eq. (A.7), we adopt a Newton Raphson iteration, rephrase it in residual form,

$$\mathrm{R}_a = \epsilon^e_{ia} - [\epsilon^e_{ia}]_{tr} + \frac{\Delta t}{2\eta_i} \tau_{ia} \doteq 0, \tag{A.8}$$

and calculate its tangent,

$$\mathrm{K}_{ab} = \frac{\partial \mathrm{R}_a}{\partial \epsilon^e_{ib}} = \delta_{ab} + \frac{\Delta t}{2\eta_i} \frac{\partial \tau_{ia}}{\partial \epsilon^e_{ib}}, \tag{A.9}$$

where

$$\begin{aligned} \frac{\partial \tau_{ia}}{\partial \epsilon^e_{ia}} &= 2\mu_i \left[+\frac{4}{9} (\tilde{\lambda}^e_{ia})^{\alpha_i} + \frac{1}{9} (\tilde{\lambda}^e_{ib})^{\alpha_i} + \frac{1}{9} (\tilde{\lambda}^e_{ic})^{\alpha_i} \right] \\ \frac{\partial \tau_{ia}}{\partial \epsilon^e_{ib}} &= 2\mu_i \left[-\frac{2}{9} (\tilde{\lambda}^e_{ia})^{\alpha_i} - \frac{2}{9} (\tilde{\lambda}^e_{ib})^{\alpha_i} + \frac{1}{9} (\tilde{\lambda}^e_{ic})^{\alpha_i} \right], \end{aligned} \tag{A.10}$$

for $a \neq b, a \neq c$, and $b \neq c$. We iteratively update the elastic logarithmic principle stretches, $[\epsilon^e_{ia}] \leftarrow [\epsilon^e_{ia}] - \sum_{b=1}^{3} \mathrm{K}^{-1}_{ab} \mathrm{R}_b$, and iterate until the residual is smaller than a user-defined tolerance, $||\mathrm{R}_a|| <$tol. At equilibrium, we update and store the internal variables, $(\mathbf{C}^v_i)^{-1} = \mathbf{F}^{-1} \cdot \mathbf{b}^e_i \cdot \mathbf{F}^{-t}$. Finally, we calculate the equilibrium Kirchhoff stress $\boldsymbol{\tau}^{eq}$ using Eq. (15), the non-equilibrium Kirchhoff stress $\boldsymbol{\tau}^{neq}$ using Eq. (13) with the individual contributiosn $\boldsymbol{\tau}_i$ from Eq. (17), the deviatoric Piola stress $\tilde{\mathbf{P}} = [\boldsymbol{\tau}^{eq} + \boldsymbol{\tau}^{neq}] \cdot \mathbf{F}^{-t}$, and the shear stress $P^{\psi}_{xz} = \tilde{P}(1,3)$ or $P^{\psi}_{yz} = \tilde{P}(2,3)$, or the compressive or tensile stress $P^{\psi}_{zz} = \tilde{P}(3,3) - pF^{-t}(3,3)$, where, for the latter, we also need to include the incompressibility constraint, $-pF^{-t}(3,3)$. Table A.8 summarizes our algorithm for the implicit time integration with exponential update.

Table A.8
Algorithm for implicit exponential time integration.

given $\mathbf{F}$ from experimental data (2) or (4)
initialize $(\mathbf{C}_i^{\mathrm{v}})^{-1} \leftarrow (\mathbf{C}_{i,\mathrm{n}}^{\mathrm{v}})^{-1}$

for each Maxwell element $i = 1, ..., m$

elastic predictor step
calculate $[\mathbf{b}_i^{\mathrm{e}}]_{\mathrm{tr}} = \mathbf{F} \cdot (\mathbf{C}_i^{\mathrm{v}})^{-1} \cdot \mathbf{F}^{\mathrm{t}}$ (A.2)
calculate $[\lambda_{i\,\mathrm{a}}^{\mathrm{e}}]_{\mathrm{tr}}$ from $[\mathbf{b}_i^{\mathrm{e}}]_{\mathrm{tr}} = \sum_{\mathrm{a}=1}^{3} [\lambda_{i\mathrm{a}}^{\mathrm{e}}]_{\mathrm{tr}}^2 [\mathbf{n}_{i\mathrm{a}}^{\mathrm{e}}]_{\mathrm{tr}} \otimes [\mathbf{n}_{i\mathrm{a}}^{\mathrm{e}}]_{\mathrm{tr}}$
calculate $[\epsilon_{i\,\mathrm{a}}^{\mathrm{e}}]_{\mathrm{tr}} = \ln [\lambda_{i\,\mathrm{a}}^{\mathrm{e}}]_{\mathrm{tr}}$ (A.7)

inelastic corrector step
local Newton iteration
calculate residual $\mathsf{R}_{\mathrm{a}} = \epsilon_{i\,\mathrm{a}}^{\mathrm{e}} - [\epsilon_{i\,\mathrm{a}}^{\mathrm{e}}]_{\mathrm{tr}} + \tau_{i\,\mathrm{a}}/2\eta_i \, \Delta t$
calculate tangent $\mathsf{K}_{\mathrm{ab}} = \partial R_{\mathrm{a}}/\partial \epsilon_{i\,\mathrm{b}}^{\mathrm{e}}$ (A.9)
update $[\epsilon_{i\,\mathrm{a}}^{\mathrm{e}}] \leftarrow [\epsilon_{i\,\mathrm{a}}^{\mathrm{e}}] - \sum_{\mathrm{b}=1}^{3} \mathsf{K}_{\mathrm{ab}}^{-1} \mathsf{R}_{\mathrm{b}}$
check convergence $||\mathsf{R}_{\mathrm{a}}|| <$ tol ?

calculate $\lambda_{i\,\mathrm{a}}^{\mathrm{e}} = \exp(\epsilon_{i\,\mathrm{a}}^{\mathrm{e}})$ (A.7)
calculate $\mathbf{b}_i^{\mathrm{e}} = \sum_{\mathrm{a}=1}^{3} (\lambda_{i\mathrm{a}}^{\mathrm{e}})^2 [\mathbf{n}_{i\mathrm{a}}^{\mathrm{e}}]_{\mathrm{tr}} \otimes [\mathbf{n}_{i\mathrm{a}}^{\mathrm{e}}]_{\mathrm{tr}}$ (8)
calculate $\boldsymbol{\tau}_i = \boldsymbol{\tau}_i(\tilde{\lambda}_{i\,\mathrm{a}}^{\mathrm{e}})$ with $\tilde{\lambda}_{i\,\mathrm{a}}^{\mathrm{e}} = (J_i^{\mathrm{e}})^{-1/3} \lambda_{i\,\mathrm{a}}^{\mathrm{e}}$ (17)

update $(\mathbf{C}_i^{\mathrm{v}})^{-1} = \mathbf{F}^{-1} \cdot \mathbf{b}_i^{\mathrm{e}} \cdot \mathbf{F}^{-\mathrm{t}}$ (8)

calculate equilibrium stress $\boldsymbol{\tau}^{\mathrm{eq}} = \boldsymbol{\tau}^{\mathrm{eq}}(\lambda_{\mathrm{a}})$ (15)
calculate non-equilibrium stress $\boldsymbol{\tau}^{\mathrm{neq}} = \sum_{i=1}^{n} \boldsymbol{\tau}_i$ (13)
calculate deviatoric Piola stress $\tilde{\mathbf{P}} = [\boldsymbol{\tau}^{\mathrm{eq}} + \boldsymbol{\tau}^{\mathrm{neq}}] \cdot \mathbf{F}^{\mathrm{t}}$

if shear
calculate $P_{xz}^{\psi} = \tilde{P}(1,3)$ and $P_{yz}^{\psi} = \tilde{P}(2,3)$

if compression/tension
calculate Lagrange multiplier $p = \tilde{P}(2,2)/F^{-\mathrm{t}}(2,2)$
calculate $P_{zz}^{\psi} = \tilde{P}(3,3) - p\,F^{-\mathrm{t}}(3,3)$

Table A.9
Algorithm for explicit time integration.

given $\mathbf{F}$ from experimental data (2) or (4)
initialize $\mathbf{C}_i^{\mathrm{v}} \leftarrow \mathbf{C}_{i,\mathrm{n}}^{\mathrm{v}}$ and $\dot{\mathbf{C}}_i^{\mathrm{v}} \leftarrow \dot{\mathbf{C}}_{i,\mathrm{n}}^{\mathrm{v}}$

for each Maxwell element $i = 1, ..., m$

elastic predictor step
calculate $\mathbf{C}_i^{\mathrm{v}\star} = \mathbf{C}_i^{\mathrm{v}} + \dot{\mathbf{C}}_i^{\mathrm{v}} \Delta t$ (A.12)
calculate $\mathbf{b}_i^{\mathrm{e}\star} = \mathbf{F} \cdot (\mathbf{C}_i^{\mathrm{v}\star})^{-1} \cdot \mathbf{F}^{\mathrm{t}}$ (8)
calculate $\lambda_{i\,\mathrm{a}}^{\mathrm{e}\star}$ from $\mathbf{b}_i^{\mathrm{e}\star} = \sum_{\mathrm{a}=1}^{3} (\lambda_{i\,\mathrm{a}}^{\mathrm{e}\star})^2 \, \mathbf{n}_{i\,\mathrm{a}}^{\mathrm{e}} \otimes \mathbf{n}_{i\,\mathrm{a}}^{\mathrm{e}}$ (9)
calculate $\boldsymbol{\tau}_i^{\star} = \boldsymbol{\tau}_i^{\star}(\tilde{\lambda}_{i\,\mathrm{a}}^{\mathrm{e}\star})$ with $\tilde{\lambda}_{i\,\mathrm{a}}^{\mathrm{e}\star} = (J_i^{\mathrm{e}\star})^{-1/3} \lambda_{i\,\mathrm{a}}^{\mathrm{e}\star}$ (17)
calculate $\mathbf{d}_i^{\mathrm{v}\star} = \boldsymbol{\tau}_i^{\star}/2\eta_i$ (20)
calculate $\dot{\mathbf{C}}_i^{\mathrm{v}\star} = 2\,\mathbf{F}^{\mathrm{t}} \cdot [\,(\mathbf{b}_i^{\mathrm{e}\star})^{-1} \cdot \mathbf{d}_i^{\mathrm{v}\star}\,]^{\mathrm{sym}} \cdot \mathbf{F}$ (A.11)

update $\mathbf{C}_i^{\mathrm{v}} = \mathbf{C}_i^{\mathrm{v}} + \frac{1}{2}\,[\,\dot{\mathbf{C}}_i^{\mathrm{v}} + \dot{\mathbf{C}}_i^{\mathrm{v}\star}\,]\,\Delta t$ (A.13)

inelastic corrector step
calculate $\mathbf{b}_i^{\mathrm{e}} = \mathbf{F} \cdot (\mathbf{C}_i^{\mathrm{v}})^{-1} \cdot \mathbf{F}^{\mathrm{t}}$ (8)
calculate $\lambda_{i\,\mathrm{a}}^{\mathrm{e}}$ from $\mathbf{b}_i^{\mathrm{e}} = \sum_{\mathrm{a}=1}^{3} (\lambda_{i\,\mathrm{a}}^{\mathrm{e}})^2 \, \mathbf{n}_{i\,\mathrm{a}}^{\mathrm{e}} \otimes \mathbf{n}_{i\,\mathrm{a}}^{\mathrm{e}}$ (9)
calculate $\boldsymbol{\tau}_i = \boldsymbol{\tau}_i(\tilde{\lambda}_{i\,\mathrm{a}}^{\mathrm{e}})$ with $\tilde{\lambda}_{i\,\mathrm{a}}^{\mathrm{e}} = (J_i^{\mathrm{e}})^{-1/3} \lambda_{i\,\mathrm{a}}^{\mathrm{e}}$ (17)
calculate $\mathbf{d}_i^{\mathrm{v}} = \boldsymbol{\tau}_i/2\eta_i$ (20)

update $\dot{\mathbf{C}}_i^{\mathrm{v}} = 2\,\mathbf{F}^{\mathrm{t}} \cdot [\,(\mathbf{b}_i^{\mathrm{e}})^{-1} \cdot \mathbf{d}_i^{\mathrm{v}}\,]^{\mathrm{sym}} \cdot \mathbf{F}$ (A.11)

calculate equilibrium stress $\boldsymbol{\tau}^{\mathrm{eq}} = \boldsymbol{\tau}^{\mathrm{eq}}(\lambda_{\mathrm{a}})$ (15)
calculate non-equilibrium stress $\boldsymbol{\tau}^{\mathrm{neq}} = \sum_{i=1}^{n} \boldsymbol{\tau}_i$ (13)
calculate deviatoric Piola stress $\tilde{\mathbf{P}} = [\,\boldsymbol{\tau}^{\mathrm{eq}} + \boldsymbol{\tau}^{\mathrm{neq}}\,] \cdot \mathbf{F}^{\mathrm{t}}$

if shear
calculate $P_{xz}^{\psi} = \tilde{P}(1,3)$ and $P_{yz}^{\psi} = \tilde{P}(2,3)$

if compression/tension
calculate Lagrange multiplier $p = \tilde{P}(2,2)/F^{-\mathrm{t}}(2,2)$
calculate $P_{zz}^{\psi} = \tilde{P}(3,3) - p\,F^{-\mathrm{t}}(3,3)$

A.2. Explicit time integration

As an alternative to the exponential time integration, we also implemented an explicit time integration scheme to advance the viscoelastic constitutive equations in time. Again, we divide the testing period of interest into discrete time intervals $t \in [t_{\mathrm{n}}, t]$ with $\Delta t = t - t_{\mathrm{n}} \geqslant 0$, where we denote all quantities of the previous time step through the subscript $(\circ)_{\mathrm{n}}$ and neglect the subscript $(\circ)_{\mathrm{n+1}}$ for all current time quantities for notational simplicity. From the experiments, we know the deformation gradient $\mathbf{F}$ of the current time step t. From the discrete time integration, we know the internal variables, the viscous right Cauchy-Green deformation tensors $\mathbf{C}_{i,\mathrm{n}}^{\mathrm{v}}$ and and their rates $\dot{\mathbf{C}}_{i,\mathrm{n}}^{\mathrm{v}}$ for all i modes, from the previous time step t_{n}. Prior to the first time step, we initialize $\mathbf{C}_{i,0}^{\mathrm{v}} = \mathbf{I}$ and $\dot{\mathbf{C}}_{i,0}^{\mathrm{v}} = \mathbf{0}$. Central to the explicit time integration is the evolution equation for the viscous right Cauchy-Green deformation tensor, which, under the assumption of a spin-free viscous deformation, $\mathbf{w}_i^{\mathrm{v}} = 0$, becomes

$$\dot{\mathbf{C}}_i^{\mathrm{v}} = 2 \cdot \mathbf{F}^{\mathrm{t}} \cdot [\,(\mathbf{b}_i^{\mathrm{e}})^{-1} \cdot \mathbf{d}_i^{\mathrm{v}}\,]^{\mathrm{sym}} \cdot \mathbf{F}. \tag{A.11}$$

We integrate this evolution equation explicitly using the Heuns method, an improved Euler method, based on a predictor and a corrector step. In the *predictor step*, indicated by the superscript $(\circ)^{\star}$, we determine the predictor of the viscous right Cauchy-Green deformation tensor,

$$\mathbf{C}_i^{\mathrm{v}\star} = \mathbf{C}_i^{\mathrm{v}} + \dot{\mathbf{C}}_i^{\mathrm{v}} \Delta t, \tag{A.12}$$

using the classical Euler forward method. With it, we calculate the predictor of the elastic left Cauchy-Green deformation tensor, $\mathbf{b}_i^{\mathrm{e}\star} = \mathbf{F} \cdot (\mathbf{C}_i^{\mathrm{v}\star})^{-1} \cdot \mathbf{F}^{\mathrm{t}}$, the predictor of the Kirchhoff stress, $\boldsymbol{\tau}_i^{\star} = \boldsymbol{\tau}_i^{\star}(\tilde{\lambda}_{i\mathrm{a}}^{\mathrm{e}\star})$, the predictor of the viscous stretch rate, $\mathbf{d}_i^{\mathrm{v}\star} = \boldsymbol{\tau}_i^{\star}/2\eta_i$, and, last, the predictor of the rate of the viscous right Cauchy-Green tensor, $\dot{\mathbf{C}}_i^{\mathrm{v}\star} = 2\,\mathbf{F}^{\mathrm{t}} \cdot [\,(\mathbf{b}_i^{\mathrm{e}\star})^{-1} \cdot \mathbf{d}_i^{\mathrm{v}\star}\,]^{\mathrm{sym}} \cdot \mathbf{F}$. In the *corrector step*, we use this rate to more accurately determine the viscous right Cauchy-Green deformation tensor,

$$\mathbf{C}_i^{\mathrm{v}} = \mathbf{C}_i^{\mathrm{v}} + \frac{1}{2}\,[\,\dot{\mathbf{C}}_i^{\mathrm{v}} + \dot{\mathbf{C}}_i^{\mathrm{v}\star}\,]\,\Delta t, \tag{A.13}$$

using the trapezoidal rule. With this corrected viscous right Cauchy-Green deformation tensor, we calculate the corrected elastic left Cauchy-Green deformation tensor, $\mathbf{b}_i^{\mathrm{e}} = \mathbf{F} \cdot (\mathbf{C}_i^{\mathrm{v}})^{-1} \cdot \mathbf{F}^{\mathrm{t}}$, the corrected Kirchhoff stress, $\boldsymbol{\tau}_i = \boldsymbol{\tau}_i(\tilde{\lambda}_{i\mathrm{a}}^{\mathrm{e}})$, the corrected viscous stretch rate, $\mathbf{d}_i^{\mathrm{v}} = \boldsymbol{\tau}_i/2\eta_i$ and, last, the corrected rate of the viscous right Cauchy-Green tensor, $\dot{\mathbf{C}}_i^{\mathrm{v}} = 2\,\mathbf{F}^{\mathrm{t}} \cdot [\,(\mathbf{b}_i^{\mathrm{e}})^{-1} \cdot \mathbf{d}_i^{\mathrm{v}}\,]^{\mathrm{sym}} \cdot \mathbf{F}$. We then store the internal variables, the viscous right Cauchy-Green tensor $\mathbf{C}_i^{\mathrm{v}}$ and its rate $\dot{\mathbf{C}}_i^{\mathrm{v}}$, for the next time increment. Finally, similar to the exponential algorithm, we calculate the equilibrium stress $\boldsymbol{\tau}^{\mathrm{eq}}$ using Eq. (15), the non-equilibrium stress $\boldsymbol{\tau}^{\mathrm{neq}}$ using Eq. (17), the deviatoric Piola stress $\tilde{\mathbf{P}} = [\,\boldsymbol{\tau}^{\mathrm{eq}} + \boldsymbol{\tau}^{\mathrm{neq}}\,] \cdot \mathbf{F}^{-\mathrm{t}}$, and the shear stress $P_{xz}^{\psi} = \tilde{P}(1,3)$ or $P_{yz}^{\psi} = \tilde{P}(2,3)$, or the compressive or tensile stress $P_{zz}^{\psi} = \tilde{P}(3,3) - pF^{-\mathrm{t}}(3,3)$, where, for the latter, we also need to include the incompressibility constraint, $-pF^{-\mathrm{t}}(3,3)$. Table A.9 summarizes our algorithm for the implicit time integration with exponential update.

References

[1] A. Goriely, M.G. Geers, G.A. Holzapfel, J. Jayamohan, A. Jérusalem, S. Sivaloganathan, W. Squier, J.A. van Dommelen, S. Waters, E. Kuhl, Mechanics of the brain: perspectives, challenges, and opportunities, Biomech. Model. Mechanobiol. 14 (2015) 931–965.

[2] J. Weickenmeier, C. Butler, P. Young, A. Goriely, E. Kuhl, The mechanics of decompressive craniectomy: personalized simulations, Comput. Methods Appl. Mech. Eng. 314 (2017) 180–195.

[3] R.J. Cloots, J. Van Dommelen, S. Kleiven, M. Geers, Multi-scale mechanics of traumatic brain injury: predicting axonal strains from head loads, Biomech. Model. Mechanobiol. 12 (2013) 137–150.

[4] C.C. Ploch, C.S. Mansi, J. Jayamohan, E. Kuhl, Using 3d printing to create personalized brain models for neurosurgical training and preoperative planning, World Neurosurgery 90 (2016) 668–674.

[5] S. Budday, A. Goriely, E. Kuhl, Neuromechanics: from neurons to brain, Adv. Appl. Mech. 48 (2015) 79–139.

[6] C.T. McKee, J.A. Last, P. Russell, C.J. Murphy, Indentation versus tensile measurements of young's modulus for soft biological tissues, Tissue Eng. Part B: Rev. 17 (2011) 155–164.

[7] S. Chatelin, A. Constantinesco, R. Willinger, Fifty years of brain tissue mechanical testing, Biorheology (2010) 255–276.

[8] K. Miller, K. Chinzei, Mechanical properties of brain tissue in tension, J. Biomech. 35 (2002) 483–490.

[9] G. Franceschini, D. Bigoni, P. Regitnig, G.A. Holzapfel, Brain tissue deforms similarly to filled elastomers and follows consolidation theory, J. Mech. Phys. Solids 54 (2006) 2592–2620.

[10] S. Budday, G. Sommer, C. Birkl, C. Langkammer, J. Haybaeck, J. Kohnert, M. Bauer, F. Paulsen, P. Steinmann, E. Kuhl, G. Holzapfel, Mechanical characterization of human brain tissue, Acta Biomater. 48 (2017) 319–340.

[11] G. Fallenstein, V.D. Hulce, J.W. Melvin, Dynamic mechanical properties of human brain tissue, J. Biomech. 2 (1969) 217–226.

[12] J.E. Galford, J.H. McElhaney, A viscoelastic study of scalp, brain, and dura, J. Biomech. 3 (1970) 211–221.

[13] L. Shuck, S. Advani, Rheological response of human brain tissue in shear, J. Basic Eng. 94 (1972) 905–911.

[14] B. Donnelly, J. Medige, Shear properties of human brain tissue, J. Biomech. Eng. 119 (1997) 423–432.

[15] A.E. Forte, S.M. Gentleman, D. Dini, On the characterization of the heterogeneous mechanical response of human brain tissue, Biomech. Model. Mechanobiol. (2017), http://dx.doi.org/10.1007/s10237-016-0860-8.

[16] L.E. Bilston, Z. Liu, N. Phan-Thien, Large strain behaviour of brain tissue in shear: some experimental data and differential constitutive model, Biorheology 38 (2001) 335–345.

[17] M. Hrapko, J. Van Dommelen, G. Peters, J. Wismans, The mechanical behaviour of brain tissue: large strain response and constitutive modelling, Biorheology 43 (2006) 623–636.

[18] T.P. Prevost, A. Balakrishnan, S. Suresh, S. Socrate, Biomechanics of brain tissue, Acta Biomater. 7 (2011) 83–95.

[19] K. Miller, K. Chinzei, Constitutive modelling of brain tissue: experiment and theory, J. Biomech. 30 (1997) 1115–1121.

[20] B. Rashid, M. Destrade, M.D. Gilchrist, Mechanical characterization of brain tissue in simple shear at dynamic strain rates, J. Mech. Behav. Biomed. Mater. 28 (2013) 71–85.

[21] A.F. Christ, K. Franze, H. Gautier, P. Moshayedi, J. Fawcett, R.J. Franklin, R.T. Karadottir, J. Guck, Mechanical difference between white and gray matter in the rat cerebellum measured by scanning force microscopy, J. Biomech. 43 (2010) 2986–2992.

[22] J. Van Dommelen, T. Van der Sande, M. Hrapko, G. Peters, Mechanical properties of brain tissue by indentation: interregional variation, J. Mech. Behav. Biomed. Mater. 3 (2010) 158–166.

[23] S. Budday, R. Nay, R. de Rooij, P. Steinmann, T. Wyrobek, T.C. Ovaert, E. Kuhl, Mechanical properties of gray and white matter brain tissue by indentation, J. Mech. Behav. Biomed. Mater. 46 (2015) 318–330.

[24] X. Jin, F. Zhu, H. Mao, M. Shen, K.H. Yang, A comprehensive experimental study on material properties of human brain tissue, J. Biomech. 46 (2013) 2795–2801.

[25] J. Weickenmeier, R. de Rooij, S. Budday, P. Steinmann, T. Ovaert, E. Kuhl, Brain stiffness increases with myelin content, Acta Biomater. 42 (2016) 265–272.

[26] M.T. Prange, S.S. Margulies, Regional, directional, and age-dependent properties of the brain undergoing large deformation, J. Biomech. Eng. 124 (2002) 244–252.

[27] K.M. Labus, C.M. Puttlitz, Viscoelasticity of brain corpus callosum in biaxial tension, J. Mech. Phys. Solids 96 (2016) 591–604.

[28] M. Kaliske, H. Rothert, Formulation and implementation of three-dimensional viscoelasticity at small and finite strains, Comput. Mech. 19 (1997) 228–239.

[29] R. de Rooij, E. Kuhl, Constitutive modeling of brain tissue: current perspectives, Appl. Mech. Rev. 68 (2016) 010801.

[30] F. Sidoroff, Nonlinear viscoelastic model with intermediate configuration, J. Mec. 13 (1974) 679–713.

[31] J. Simo, Algorithms for static and dynamic multiplicative plasticity that preserve the classical return mapping schemes of the infinitesimal theory, Comput. Methods Appl. Mech. Eng. 99 (1992) 61–112.

[32] S. Reese, S. Govindjee, A theory of finite viscoelasticity and numerical aspects, Int. J. Solids Struct. 35 (1998) 3455–3482.

[33] A. Jérusalem, M. Dao, Continuum modeling of a neuronal cell under blast loading, Acta Biomater. 8 (2012) 3360–3371.

[34] G.E. Lang, P.E. Stewart, D. Vella, S.L. Waters, A. Goriely, Is the donnan effect sufficient to explain swelling in brain tissue slices?, J R. Soc. Interface 11 (2014) 20140123.

[35] G. Sommer, M. Eder, L. Kovacs, H. Pathak, L. Bonitz, C. Mueller, P. Regitnig, G.A. Holzapfel, Multiaxial mechanical properties and constitutive modeling of human adipose tissue: a basis for preoperative simulations in plastic and reconstructive surgery, Acta Biomater. 9 (2013) 9036–9048.

[36] G.A. Holzapfel, J.C. Simo, A viscoelastic constitutive model for continuous media at finite thermomechanical changes, Int. J. Solids Struct. 33 (1996) 3019–3034.

[37] R. Ogden, Large deformation isotropic elasticity-on the correlation of theory and experiment for incompressible rubberlike solids, Proc. R. Soc. London A 326 (1972) 565–584.

[38] S. Govindjee, S. Reese, A presentation and comparison of two large deformation viscoelastic models, J. Eng. Mater. Technol. 119 (1997) 251–255.

[39] M.C. Boyce, D.M. Parks, A.S. Argon, Large inelastic deformation of glassy polymers. Part i: rate dependent constitutive model, Mech. Mater. (1988) 15–33.

[40] G. Weber, L. Anand, Finite deformation constitutive equations and a time integration procedure for isotropic, hyperelastic-viscoplastic solids, Comput. Methods Appl. Mech. Eng. 79 (1990) 173–202.

[41] J. Bonet, Large strain viscoelastic constitutive models, Int. J. Solids Struct. (2001) 2953–2968.

[42] F. Vogel, S. Göktepe, P. Steinmann, E. Kuhl, Modeling and simulation of viscous electro-active polymers, Eur. J. Mech. A/Solids (2014) 112–128.

[43] B. Rashid, M. Destrade, M.D. Gilchrist, Mechanical characterization of brain tissue in tension at dynamic strain rates, J. Mech. Behav. Biomed. Mater. 33 (2014) 43–54.

[44] B. Rashid, M. Destrade, M.D. Gilchrist, Mechanical characterization of brain tissue in compression at dynamic strain rates, J. Mech. Behav. Biomed. Mater. 10 (2012) 23–38.

[45] L.A. Mihai, L. Chin, P.A. Janmey, A. Goriely, A comparison of hyperelastic constitutive models applicable to brain and fat tissues, J. R. Soc. Interface 12 (2015) 20150486.

[46] K. Pogoda, L. Chin, P.C. Georges, F.J. Byfield, R. Bucki, R. Kim, M. Weaver, R.G. Wells, C. Marcinkiewicz, P.A. Janmey, Compression stiffening of brain and its effect on mechanosensing by glioma cells, New J. Phys. 16 (2014) 075002. Combined loading, small strains, mouse..

[47] L. Mihai, S. Budday, G. Holzapfel, E. Kuhl, A. Goriely, A family of hyperelastic models for human brain tissue, J. Mech. Phys. Solids 106 (2017) 60–79.

[48] K. Miller, Constitutive model of brain tissue suitable for finite element analysis of surgical procedures, J. Biomech. 32 (1999) 531–537.

[49] A. Gefen, N. Gefen, Q. Zhu, R. Raghupathi, S.S. Margulies, Age-dependent changes in material properties of the brain and braincase of the rat, J. Neurotrauma 20 (2003) 1163–1177.

[50] A. Tamura, S. Hayashi, I. Watanabe, K. Nagayama, T. Matsumoto, Mechanical characterization of brain tissue in high-rate compression, J. Biomech. Sci. Eng. 2 (2007) 115–126.

[51] B.S. Elkin, B. Morrison, Viscoelastic properties of the P17 and adult rat brain from indentation in the coronal plane, J. Biomech. Eng. 135 (2013) 114507.

[52] L.E. Bilston, Neural Tissue Biomechanics, Springer, Heidelberg, 2011.

[53] W. Ehlers, A. Wagner, Multi-component modelling of human brain tissue: a contribution to the constitutive and computational description of deformation, flow and diffusion processes with application to the invasive drug-delivery problem, Comput. Methods Biomech. Biomed. Eng. 18 (2015) 861–879.

[54] S. Cheng, L.E. Bilston, Unconfined compression of white matter, J. Biomech. 40 (2007) 117–124.

[55] Y. Feng, R.J. Okamoto, R. Namani, G.M. Genin, P.V. Bayly, Measurements of mechanical anisotropy in brain tissue and implications for transversely isotropic material models of white matter, J. Mech. Behav. Biomed. Mater. 23 (2013) 117–132.

[56] D.E. Koser, E. Moeendarbary, J. Hanne, S. Kuerten, K. Franze, CNS cell distribution and axon orientation determine local spinal cord mechanical properties, Biophys. J . 108 (2015) 2137–2147.

[57] E. Bar-Kochba, M. Scimone, J. Estrada, C. Franck, Strain and rate-dependent neuronal injury in a 3D in vitro compression model of traumatic brain injury, Sci. Rep. 6 (2016) 30550.

[58] A. Bain, D. Meaney, Axonal damage in an experimental model of central nervous system white matter injury, J. Biomech. Eng. 122 (2000) 615–622.

[59] S. Budday, P. Steinmann, E. Kuhl, The role of mechanics during brain development, J. Mech. Phys. Solids 72 (2014) 75–92.

[60] A. Gefen, S.S. Margulies, Are in vivo and in situ brain tissues mechanically similar?, J Biomech. 37 (2004) 1339–1352.

[61] T.P. Prevost, G. Jin, M.A. de Moya, H.B. Alam, S. Subresh, S. Socrate, Dynamic mechanical response of brain tissue in indentation in vivo, in situ and in vitro, Acta Biomater. 7 (2011) 4090–4101.

[62] Y.K. Mariappan, K.J. Glaser, R.L. Ehman, Magnetic resonance elastography: a review, Clin. Anat. 23 (2010) 497–511.

[63] S.A. Kruse, G.H. Rose, K.J. Glaser, A. Manduca, J.P. Felmlee, C.R. Jack, R.L. Ehman, Magnetic resonance elastography of the brain, Neuroimage 39 (2008) 231–237. Elastography white stiffer gray..

[64] K.J. Glaser, A. Manduca, R.L. Ehman, Review of MR elastography applications and recent developments, J. Magn. Reson. Imaging 36 (2012) 757–774.

[65] J. Weickenmeier, M. Kurt, E. Ozkaya, M. Wintermark, K. Butts Pauly, E. Kuhl, Magnetic resonance elastography of the brain: a comparison between pigs and humans, submitted (2017).